

# Physics of 1 keV line in X-ray binaries

Priyanka Chakraborty<sup>1\*</sup>, Gary Ferland<sup>2</sup>, Andrew Fabian<sup>3</sup>, Arnab Sarkar<sup>4</sup>, Renee Ludlam<sup>5</sup>, Stefano Bianchi<sup>6</sup>, Hayden Hall<sup>5</sup>, Peter Kosec<sup>1</sup>

<sup>1</sup>Center for Astrophysics|Harvard & Smithsonian, Cambridge, MA

<sup>2</sup>University of Kentucky, Lexington, KY, USA

<sup>3</sup>Institute of Astronomy, Madingley road, Cambridge CB3 0HA, UK

<sup>4</sup>Kavli Institute for Astrophysics and Space Research, Massachusetts Institute of Technology, Cambridge, MA

<sup>5</sup>Department of Physics and Astronomy, Wayne State University, 666 W. Hancock St., 48201, Detroit, MI, USA

<sup>6</sup>Dipartimento di Matematica e Fisica, Università degli Studi Roma Tre, via della Vasca Navale 84, I-00146 Roma, Italy

Accepted XXX. Received YYY; in original form ZZZ

## ABSTRACT

X-ray binaries (XRBs) often exhibit spectral residuals in the 0.5 to 2 keV range, known as the “1 keV residual/1 keV feature”, with variable centroid and intensity across different systems. Yet a comprehensive scientific explanation of the variability of the 1 keV feature has remained largely elusive. In this paper, we explain for the first time the origin and variability of the 1 keV feature in XRBs using the spectral synthesis code *CLOUDY*. We constructed line blends for the emission and absorption lines and study the variability of these blends with ionization parameters, temperature, and column density. We conducted a sample study involving five XRBs including two ultraluminous X-ray sources (ULXs): NGC 247 ULX-1, NGC 1313 X-1, a binary X-ray pulsar : Hercules X-1, and two typical low-mass X-ray binaries (LMXBs): Cygnus X-2, and Serpens X-1, providing a comprehensive explanation of the 1 keV feature observed across these targets.

**Key words:** X-ray binary, Ultraluminous X-ray sources (ULXs)

## 1 INTRODUCTION

X-ray binaries (XRBs) feature a compact object (white dwarf, neutron star, or black hole) accreting from a stellar companion, harnessing gravitational energy release for power. XRBs often exhibit spectral features, commonly referred to as the “1 keV residuals,” within the energy range of 0.5 to 2 keV. These features have been ubiquitously observed in various types of X-ray binaries, including ultraluminous X-ray sources (ULXs) (Stobbart et al. 2006; Roberts et al. 2006; Middleton et al. 2015; Pinto et al. 2020), X-ray pulsars (Malacaria et al. 2023; Schwöpe et al. 2023), and typical low-mass X-ray binaries (LMXBs) (Asai et al. 2000; Iaria et al. 2016; Ludlam et al. 2018; Kosec et al. 2021), over the course of several decades. Interestingly, both the centroid and intensity of this feature exhibit variations, not only across different binaries but also over time within the same binary (Paul et al. 2002; Walton et al. 2020). Despite scattered attempts to model the 1 keV feature using various approaches, a comprehensive explanation for the origin and variability of these residuals has proven challenging to ascertain. In this paper, we present a comprehensive model aimed at understanding the physics of this feature. We investigate various scenarios, including collisionally-ionized, photoionized, and reflective origins of the feature, while also examining the variability of their centroids and intensity. We demonstrate the application of our model on a diverse array of X-ray binaries, including ULXs (NGC 1313 X-1 and NGC 247 ULX-1), typical LMXBs (Cygnus X-2 and Serpens X-1), and X-ray pulsars (Hercules X-1).

## 2 SAMPLE SELECTION OVERVIEW

*NGC 1313 X-1:* NGC 1313 X-1 is one of the ULX in the starburst galaxy NGC 1313, exhibiting isotropic luminosity of  $L_X = 2.0 \times 10^{40}$  erg s<sup>-1</sup> (0.2–10.0 keV) and unusual spectral variability (Miller et al. 2003; Walton et al. 2020). Strong rest-frame emission lines around 1 keV have been detected along with blue-shifted atomic absorption features through XMM-Newton observations of NGC 1313 X-1 (Pinto et al. 2016), which was later confirmed to vary in time (Pinto et al. 2020).

*NGC 247 ULX-1:* NGC 247 ULX-1 was first identified as an ULX from a short XMM-Newton observation (Winter et al. 2006), while a second XMM-Newton observation confirmed its soft nature (Jin et al. 2011). Later, Feng et al. (2016) found that NGC 247 ULX-1 switches between supersoft ultraluminous (SSUL) and soft ultraluminous (SUL) regime (Feng et al. 2016). Pinto et al. (2021) analyzed XMM-Newton observations of NGC 247 ULX-1 for eight observations taken between 2019 and 2020 and detected 1 keV residuals that seemed to vary with each observation, both the centroid and intensity, and identified the need for a complex atomic model for correctly explaining the residuals.

*Hercules X-1:* Hercules X-1, commonly referred to as Her X-1, is one of the extensively observed accreting binary X-ray pulsars with intriguing properties. The X-ray emissions from the system exhibit three distinct timescales: the 1.24s X-ray pulsation (Feigelson 1975), the 1.7-day orbital period (Tananbaum et al. 1972), and a super-orbital 35-day cycle (Ogelman et al. 1985). The 35-day cycle of high and low flux state is believed to be induced by the precession of a twisted accretion disc. The first 1 keV residual in Hercules X-1 was

\* E-mail: priyanka.chakraborty@cfa.harvard.edu

detected through BeppoSAX observations and exhibited variability (Oosterbroek et al. 1997, 2001). A more prominent detection of 1 keV residual in both emission and absorption was achieved through a series of XMM-Newton observations in August 2020 (Kosec et al. 2022).

*Serpens X-1*: The luminous persistent LMXB Serpens X-1, abbreviated as Ser X-1, was first identified in 1965 (Bowyer et al. 1965). Type I X-ray bursts were detected from the source in 1976, confirming the presence of its neutron star accretor (Swank et al. 1976). Serpens X-1 offers a unique chance to identify numerous reflection features owing to the minimal amount of absorbing material along its line of sight. The first reflection feature detected was the Fe K complex through XMM-Newton observations (Bhattacharyya & Strohmayer 2007), with a recent detection of the Fe L complex reflection feature partly contributing to the 1 keV residual in Serpens X-1 (Ludlam et al. 2018) and emission residuals between 0.5–0.9 keV which remained unaccounted for.

*Cygnus X-2*: Cygnus X-2, often referred to as Cyg X-2, has long been recognized as a typical low-mass X-ray binary hosting a neutron star with a relatively extended orbital period of  $P = 9.84$  days (Cowley et al. 1979; Smale 1998). Over the years, several studies have identified a 1 keV feature in Cyg X-2 through Einstein, BeppoSAX, and Suzaku observatories (Vrtilek et al. 1986; Di Salvo et al. 2002; Cackett et al. 2010), with a recent study by Ludlam et al. (2022) detecting a prominent emission feature at 1 keV with minimal absorption using *NICER* observations carried out in 2019.

We used the spectral synthesis code *CLOUDY* (Ferland et al. 2017) for all our simulations. We adopted a cosmology of  $H_0 = 70 \text{ km s}^{-1} \text{ Mpc}^{-1}$ ,  $\Omega_\Lambda = 0.7$ . Unless otherwise stated, all reported error bars are at 90% confidence level.

### 3 DATA REDUCTION

#### 3.1 NGC 1313 X-1 and NGC 247 ULX-1

NGC 1313 X-1 was observed using XMM-Newton during nine distinct periods spanning from 2014 to 2017. These observations utilized both the European Photon Imaging Camera (EPIC, Turner et al. 2001) and Reflection Grating Spectrometer (RGS, den Herder et al. 2001) onboard XMM-Newton. Five out of the nine observations were reported to be in the intermediate-bright state (Pinto et al. 2020). To gain a detailed view of the 1 keV emission line complex, we utilized the RGS observations of these five brightest observations (obs ids: 0742590301, 0803990101, 0803990201, 0803990501, 0803990601), with exposure time totaling 592 ks. In our analysis of NGC 1313 X-1, we used the Spectral Energy Distribution (SED) from Vinokurov et al. (2013) for the UV and optical energy bands and the SED from Pinto et al. (2020) for the X-ray band.

NGC 247 ULX-1 was observed with XMM-Newton between 2019 and 2020, with the exposure time totaling 886 ks. For this work, we utilized all eight RGS observations of NGC 247 ULX-1, identified by observation IDs: 0844860101, 0844860201, 0844860301, 0844860401, 0844860501, 0844860601, 0844860701, and 0844860801. We adopted the SED derived from the time-averaged spectrum in the optical, UV, and X-ray bands, sourced from, and a Pinto et al. (2021). For both targets, The RGS data reduction was performed using the *rgsproc* pipeline from the Science Analysis System (sas) software package. The periods affected by contamination from solar flare were filtered using *rgsfilter*, by selecting background-quiet intervals in the lightcurves of the RGS 1 and 2 from CCD number 9. A count rate threshold of  $\sim 0.2$  c/s were applied. The clean exposure times are listed in Table 1.

For each source, we extracted the first and second ordered RGS spectra from a cross-dispersion region of  $0.8'$ . Both cross-dispersion regions were centered on the respective source coordinates—RA =  $49.58^\circ$ , DEC =  $-66.48^\circ$  for NGC 1313 X-1 and RA =  $11.76^\circ$ , DEC =  $-20.79^\circ$  for NGC 247 ULX-1. The background spectra for each source were extracted by selecting photons that extended beyond the 98% boundary of the source point-spread-function. We note that the background regions never overlapped the bright source under consideration. The *rgsproc* tool also generates the corresponding response files for RGS 1 and 2. For each source, we used the *rgscombine* tool to stack RGS 1 and 2 first-order source spectra, background spectra and corresponding response files from all the obs ids.

#### 3.2 Hercules X-1

We utilized the RGS spectrum of Hercules X-1 during its Main High state (precession phase 0.063 – 0.098, Kosec et al. 2021) from an observation with a 126.5 ks raw exposure (Obs Id: 0865440401). The data were obtained from the XSA archive and reduced using a standard pipeline with *sas v19*, *CALDB* as of 2021 June. The RGS data reduction was performed using the *rgsproc* task. A cross-dispersion region with a width of  $= 1.4'$  was adopted, centered at RA =  $254.46^\circ$  and DEC =  $35.34^\circ$ . We only used periods during which Her X-1 is in a high flux state to create the RGS spectra. For this reason, we excluded a time interval at the beginning of the observation during which Her X-1 was in eclipse, and a time interval at the end of the observation during which the source exhibited absorption dipping. We identified no background flares during this exposure. The remaining net RGS exposure time (per detector) is 104 ks. We only used 1st-order RGS data and stacked the RGS 1 and 2 spectra using the *rgscombine* routine. Energies below 0.56 keV were excluded from the fitting due to the detection of a potential instrumental residual in the 0.52–0.56 keV energy band, as detailed in Kosec et al. (2021), Appendix B. We referenced the Spectral Energy Distribution (SED) specific to this observation from Kosec et al. (2022).

#### 3.3 Cyg X-2 and Ser X-1

We utilized the 12.1 ks observation with observation ID 2631010201 from *NICER* for observations carried out in 2019. The data reduction was carried out utilizing *CALDB* version 20210427, and the source and background spectrum for the *NICER* observation were created using the ‘3C50’ tool (Remillard et al. 2022). The detailed data reduction method is described in Ludlam et al. (2022) under horizontal branch (HB), obs 3. The SED specific to this observation was taken from Ludlam et al. (2022). For Ser X-1, our analysis incorporated *NICER* data collected from July to November 2017, across ObsIDs 1050320101–1050320113, totaling an exposure of 39.9 ks. The data for Ser X-1 was processed using the same methods as Cyg X-2, using the updated *NICER* *CALDB* version xti20221001. The SED for this observation was adopted from Ludlam et al. (2018).

### 4 PHYSICS OF THE BLEND: CLOUDY MODELS

In this work, we conducted a detailed investigation into the origins of the 1 keV lines, exploring photoionized equilibrium (PIE), collisional ionization equilibrium (CIE), and reflection mechanisms. Previous observations using high-resolution spectra have shown that XRBs often exhibit strong emission residuals in the energy range between 0.6 and 1.4 keV (Middleton et al. 2014; Fabrika et al. 2021). To model the emission feature within this full energy range in *CLOUDY*,

**Table 1.** Observation log detailing the XRB sample utilized in this paper.

Target	Instrument	Observation ID	Start Date/Time	Exposure(ksec)
NGC 1313 X-1	<i>XMM-Newton</i> /RGS	0742590301	2014-07-05 22:37:13	62.99
		0803990101	2017-06-14 20:40:21	137.10
		0803990201	2017-06-20 21:06:00	133.80
		0803990501	2017-12-07 10:28:21	128.90
		0803990601	2017-12-09 10:20:09	128.90
NGC 247 ULX-1	<i>XMM-Newton</i> /RGS	0844860101	2019-12-03 12:41:51	115.50
		0844860201	2019-12-09 12:48:29	118.60
		0844860301	2019-12-09 12:48:29	119.60
		0844860401	2020-01-02 10:43:35	120.00
		0844860501	2020-01-04 10:52:05	119.00
		0844860601	2020-01-06 04:36:08	115.00
		0844860701	2020-01-06 04:36:08	115.00
		0844860801	2020-01-12 03:59:00	63.20
Her X-1	<i>XMM-Newton</i> /RGS	0865440401	2020-08-12 16:06:27	126.5
Ser X-1	<i>NICER</i>	1050320101–1050320113	2017-7 - 2017-11	39.9
Cyg X-2	<i>NICER</i>	2631010201	2019-09-12 02:09:44	12.1

we constructed an emission line blend, which we call  $\text{Em}_{\text{blend}}$  including emission lines in the 0.6–1.4 keV energy band. Further, we constructed two emission line blends by including all the emission lines between 0.6 to 1 keV and 1 keV to 1.4 keV, which we call  $\text{Em}_{\text{left}}$  and  $\text{Em}_{\text{right}}$ , respectively.

Previous observations also showed that two absorption features on either sides of the emission feature are ubiquitous among XRB spectra, particularly ULXs (Pinto et al. 2016; Wang et al. 2019). We, therefore, constructed two absorption line blends in *CLOUDY*: one comprising all the absorption lines located in the left of the 1 keV energy, designated as  $\text{Abs}_{\text{left}}$ , and another encompassing all the absorption lines at the right of the 1 keV energy, denoted as  $\text{Abs}_{\text{right}}$ . The full absorption line blend, including all absorption lines within the energy band 0.5–2.0 keV, is referred to as  $\text{Abs}_{\text{blend}}$ .

XRBs might display noticeable reflection characteristics, often characterized by the presence of the Fe L complex (Cackett et al. 2010; Ludlam et al. 2018). We created two reflection line blends within the energy interval 0.5–2.0 keV using *CLOUDY*: one containing all the reflection lines to the left of the 1 keV energy, labeled as  $\text{Reflect}_{\text{left}}$ , and another comprising all the reflection lines positioned to the right of the 1 keV energy, designated as  $\text{Reflect}_{\text{right}}$ . The reflection line blend covering the energy range of 0.5 to 2.0 keV was designated as  $\text{Reflect}_{\text{blend}}$ . Table 2 lists all the lines from  $\text{Em}_{\text{blend}}$ ,  $\text{Abs}_{\text{blend}}$ , and  $\text{Reflect}_{\text{blend}}$ , along with instructions for creating these blends within *CLOUDY* in the appendix.

The emission, absorption, and reflection line blends are expected to vary among different systems and a successful model should predict these variation to make it useful in understanding the evolution of 1 keV feature in different systems. To study how the shift of the centroid and intensity of the 1 keV emission feature vary with the different physical properties of XRBs, we examined the variation of  $\text{Em}_{\text{left}}/\text{Em}_{\text{right}}$  and  $\text{Em}_{\text{blend}}$  with a range of ionization parameters ( $\xi$ ) and hydrogen column densities ( $N_{\text{H}}$ ) in a PIE plasma. For CIE plasma, we investigated the variation  $\text{Em}_{\text{left}}/\text{Em}_{\text{right}}$  and  $\text{Em}_{\text{blend}}$  with a range of temperatures ( $T$ ) and hydrogen column densities ( $N_{\text{H}}$ ). Similarly, for absorption line blends, we examined the variation in  $\text{Abs}_{\text{left}}/\text{Abs}_{\text{right}}$  and  $\text{Abs}_{\text{blend}}$  with  $\xi$  and  $N_{\text{H}}$  to trace the shifts in the centroid and intensity of the 1 keV absorption feature. Since the absorption features have been consistently linked to a PIE wind origin

(Cackett et al. 2008; Pinto et al. 2017), we did not investigate the variation of the absorption features ( $\text{Abs}_{\text{blend}}$  and  $\text{Abs}_{\text{left}}/\text{Abs}_{\text{right}}$ ) with  $T$  or  $N_{\text{H}}$  for CIE plasma.

We found that the variation in the emission and absorption line blends with electron density was negligible ( $\leq 7\%$ ) for electron densities up to  $10^{15} \text{ cm}^{-3}$  (see Figure 7). Consequently, we did not use electron density as a variable in contour plots. Instead, we kept electron density as a free parameter for the spectral fittings discussed in Section 5.

#### 4.1 Emission lines from PIE

We utilized target-specific spectral energy distributions (SEDs) from Section 3 to generate emission lines from PIE plasma for all five targets. These SEDs were utilized as radiation sources in *CLOUDY*. Our investigation focused on understanding how  $\text{Em}_{\text{blend}}$  and  $\text{Em}_{\text{left}}/\text{Em}_{\text{right}}$  vary with two key parameters: ionization parameter ( $\xi$ ) and hydrogen column density ( $N_{\text{H}}$ ). For each XRB under consideration, we constructed a logarithmic grid for  $\xi$ , spanning log  $\xi$  values from 0.5 to 5.0, with increments of 0.1 dex. Similarly, we created a logarithmic grid for  $N_{\text{H}}$ , ranging between log  $N_{\text{H}}$  values of 20 to 24, also in 0.1 dex increments. In total, this resulted in 2000 distinct grids for our analysis.

Figure 1 and 2 illustrates the observed changes in  $\text{Em}_{\text{blend}}$  and  $\text{Em}_{\text{left}}/\text{Em}_{\text{right}}$  for the targets of our interest. In Figure 1, we displayed how  $\text{Em}_{\text{blend}}$  varies with log  $\xi$  and log  $N_{\text{H}}$ . This variation in  $\text{Em}_{\text{blend}}$  represents the alterations in the intensity of the 1 keV emission feature. The normalization of  $\text{Em}_{\text{blend}}$  is executed as follows: each value of  $\text{Em}_{\text{blend}}$  is scaled by dividing it by the maximum  $\text{Em}_{\text{blend}}$  observed within the same parameter space. This method ensures that  $\text{Em}_{\text{blend}}$  values are dimensionless, ranging from 0 to 1, thereby standardizing the data for comparative analysis across different parameter sets. Specifically, as  $\text{Em}_{\text{blend}}$  approaches 1, it indicates a stronger 1 keV emission feature, whereas  $\text{Em}_{\text{blend}} \ll 1$  signifies a diminished 1 keV emission feature. In Figure 2, we depicted the variation of  $\text{Em}_{\text{left}}/\text{Em}_{\text{right}}$  with log  $\xi$  and log  $N_{\text{H}}$ , which characterizes the shift in the centroid of the 1 keV emission feature. A ratio above 1 indicates a leftward shift of the centroid of the 1 keV feature, while

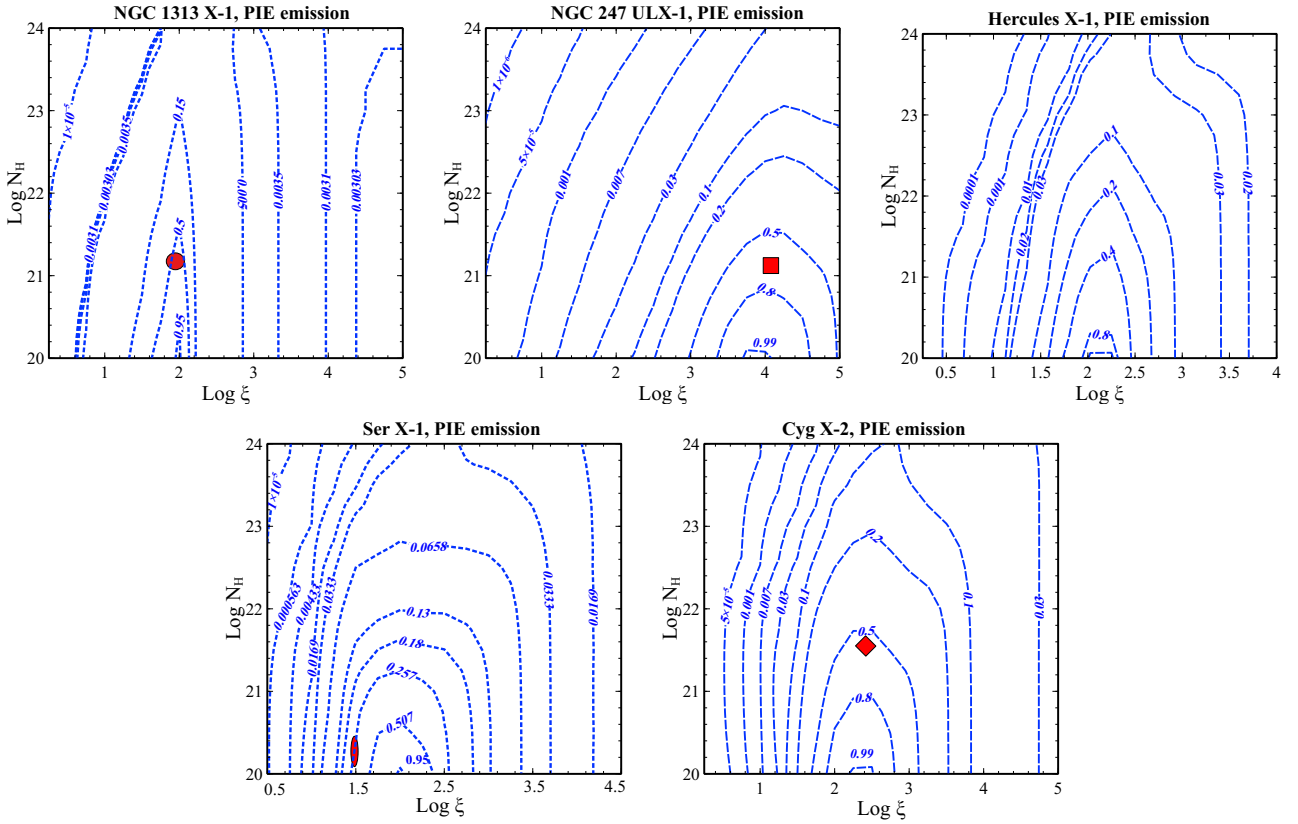
**Table 2.** List of spectral lines in the 1 keV blend. Line intensities vary depending on the shape of the SED,  $\xi$ ,  $N_{\text{H}}$ , and  $T$ .

Ion	$\lambda$ (Å)	Ion	$\lambda$ (Å)	Ion	$\lambda$ (Å)	Ion	$\lambda$ (Å)	Ion	$\lambda$ (Å)	Ion	$\lambda$ (Å)
Mg XII	6.58008	Al XII	6.63476	Si XIII	6.64803	Si XIII	6.68827	Si XIII	6.74039	Mg XII	7.10615
Al XIII	7.17271	Mg XI	7.31028	Mg XI	7.47313	Al XII	7.75730	Mg XI	7.85052	Fe XX	8.20998
Fe XX	8.27000	Fe XX	8.31000	Mg XII	8.42100	Fe XX	8.44003	Fe XX	8.46002	Fe XX	8.50000
Fe XX	8.69996	Fe XXII	8.71500	Fe XXII	8.72200	Fe XX	8.74004	Fe XX	8.77001	Fe XIX	8.81003
Fe XXI	8.84000	Fe XXI	8.85500	Fe XXI	8.89800	Fe XX	8.89996	Fe XX	8.91997	Fe XX	8.93001
Fe XIX	8.96001	Fe XXII	8.97700	Fe XIX	9.03000	Fe XX	9.06500	Fe XIX	9.06997	Fe XXII	9.07300
Fe XX	9.11000	Fe XXII	9.12200	Fe XXI	9.14000	Fe XXII	9.14800	Fe XX	9.16300	Mg XI	9.16875
Fe XX	9.18400	Fe XIX	9.18999	Fe XIX	9.19997	Fe XX	9.21600	Fe XIX	9.21999	Fe XX	9.22000
Fe XIX	9.23003	Mg XI	9.23121	Fe XX	9.25800	Fe XX	9.28100	Mg XI	9.31434	Fe XIX	9.32001
Fe XX	9.32500	Ni XXV	9.33000	Fe XIX	9.33001	Ne X	9.36162	Ni XX	9.37700	Ni XX	9.38500
Fe XIX	9.45001	Ni XX	9.45500	Fe XXI	9.47500	Ne X	9.48075	Fe XXI	9.48200	Fe XXI	9.54200
Fe XXI	9.54800	Ni XX	9.55800	Ni XX	9.55900	Fe XXI	9.58200	Fe XXI	9.58700	Fe XIX	9.63900
Fe XXI	9.69000	Fe XIX	9.69100	Fe XXI	9.70000	Fe XXI	9.70500	Ne X	9.70818	Fe XIX	9.72600
Fe XXI	9.82100	Fe XIX	9.84800	Fe XIX	9.85200	Fe XIX	9.88800	Na XI	10.02500	Fe XVIII	10.08000
Ni XIX	10.11000	Ne X	10.23890	Fe XVIII	10.41000	Fe XXIII	10.50600	Fe XVIII	10.52600	Fe XXIV	10.61900
Fe XIX	10.63200	Fe XIX	10.63300	Fe XIX	10.65500	Fe XIX	10.65700	Fe XXIV	10.66300	Fe XIX	10.68400
Fe XIX	10.70200	Cr XX	10.71200	Fe XIX	10.74400	Fe XIX	10.75800	Fe XIX	10.76000	Ni XX	10.77200
Fe XIX	10.80500	Fe XIX	10.81600	Fe XIX	10.82700	Fe XIX	10.88000	Fe XIX	10.91600	Fe XIX	10.93300
Fe XXIII	10.98000	Na X	11.00260	Fe XXIII	11.01800	Ni XX	11.13800	Ni XX	11.15800	Ni XX	11.22600
Ni XXI	11.22700	Ni XXI	11.24100	Ni XXI	11.24200	Ni XXI	11.27200	Ni XX	11.28200	Ni XXI	11.30200
Ni XXI	11.31900	Fe XVIII	11.32600	Ni XXI	11.38000	Fe XVIII	11.42000	Fe XXII	11.44200	Fe XXII	11.45900
Ni XXI	11.46800	Fe XXIII	11.48500	Fe XX	11.51000	Ni XXI	11.51600	Ni XXI	11.51700	Fe XVIII	11.52500
Ni XXI	11.53900	Ne IX	11.54660	Mn XXIII	11.57660	Ni XXI	11.59700	Fe XXII	11.59900	Fe XXII	11.66900
Fe XXIII	11.71800	Fe XXIII	11.73700	Fe XX	11.73900	Fe XXII	11.76800	Ni XX	11.78700	Ni XX	11.83200
Fe XXIII	11.84600	Ni XX	11.86500	Ni XX	11.87400	Fe XXII	11.92100	Fe XX	11.93300	Fe XXII	11.93400
Fe XXI	11.93800	Ni XX	11.96100	Mn XXII	11.97000	Fe XXI	11.97500	Ni XX	11.97800	Fe XX	11.98700
Ca XVIII	11.98900	Ni XX	11.99100	Mn XXII	11.99800	Ni XX	12.00600	Ti XIX	12.01000	Fe XXIII	12.02700
Fe XXI	12.04400	Ni XX	12.04700	Ni XX	12.08100	Fe XXI	12.08200	Fe XXI	12.10700	Ni XX	12.11200
Ni XX	12.13000	Ne X	12.13390	Fe XXI	12.14600	Ni XX	12.15700	Fe XXIII	12.16100	Ni XXI	12.16500
Fe XXII	12.19300	Ni XXI	12.20900	Fe XXI	12.26100	Ni XXI	12.27600	Fe XXI	12.28200	Fe XXI	12.29700
Fe XXI	12.32700	Fe XXIII	12.35100	Fe XXI	12.39500	Fe XXI	12.42200	Fe XX	12.42600	Ni XIX	12.43500
Fe XXIII	12.44400	Ni XXI	12.44600	Fe XXI	12.46200	Ni XXI	12.47200	Fe XXI	12.49000	Fe XXI	12.49200
Fe XXIII	12.49300	Fe XXI	12.49900	Fe XXI	12.50000	Fe XXI	12.52300	Ni XXI	12.53300	Fe XX	12.56600
Fe XXI	12.56800	Fe XX	12.58100	Ni XXI	12.59100	Cr XXII	12.61300	Fe XXI	12.62300	Ca XVIII	12.63600
Ni XXI	12.64800	Fe XXIII	12.65300	Cr XXII	12.65500	Ni XIX	12.65600	Fe XXI	12.66300	Fe XXI	12.69100
Fe XXI	12.70100	Fe XXIII	12.70300	Fe XXII	12.74300	Fe XX	12.75300	Fe XXI	12.77200	Fe XX	12.80400
Fe XX	12.81200	Fe XVIII	12.81800	Fe XXI	12.82200	Fe XX	12.82400	Fe XX	12.82700	Fe XX	12.84500
Fe XXI	12.87000	Fe XX	12.90500	Fe XIX	12.92400	Ni XX	12.92700	Fe XXII	12.93600	Fe XX	12.95100
Fe XX	12.96600	Fe XX	12.98200	Fe XX	12.99100	Fe XIX	13.01800	Ni XX	13.03200	Fe XIX	13.03900
Fe XX	13.04400	Fe XX	13.04600	Fe XIX	13.05100	Fe XX	13.05200	Fe XXI	13.05200	Fe XX	13.05900
Fe XIX	13.07500	Ni XX	13.07500	Fe XX	13.07800	Fe XX	13.09100	Fe XIX	13.09100	Fe XX	13.09100
Fe XX	13.11400	Fe XX	13.12300	Cr XXI	13.12300	Fe XX	13.14000	Fe XX	13.14300	Fe XXI	13.17900
Fe XX	13.18800	Fe XX	13.20300	Fe XX	13.20600	Fe XIX	13.21200	Fe XIX	13.21200	Fe XX	13.25300
Fe XX	13.25400	Fe XIX	13.25400	Fe XXI	13.25500	Ni XX	13.25600	Fe XX	13.26700	Fe XX	13.26900
Fe XX	13.27000	Ni XX	13.28200	Fe XX	13.29200	Fe XX	13.30100	Fe XIX	13.31100	Fe XVIII	13.31900
Fe XIX	13.32700	Fe XX	13.33300	Fe XIX	13.33600	Fe XVIII	13.35500	Fe XX	13.35900	Fe XXII	13.36100
Fe XX	13.36600	Fe XVIII	13.37400	Fe XX	13.37900	Fe XX	13.38200	Fe XVIII	13.39700	Fe XX	13.40200
Fe XX	13.40500	Fe XX	13.41900	Fe XVIII	13.42400	Fe XIX	13.43000	Ne IX	13.44710	Fe XIX	13.45600
Ca XVII	13.46000	Fe XIX	13.46200	Fe XVIII	13.46400	Fe XX	13.46700	Fe XIX	13.47100	Fe XXI	13.48200
Fe XIX	13.50600	Fe XIX	13.50700	Fe XX	13.51700	Fe XIX	13.52500	Fe XX	13.53300	Fe XIX	13.55400
Fe XIX	13.55500	Fe XIX	13.55700	Fe XXI	13.57400	Fe XXII	13.61700	Fe XIX	13.62000	Fe XIX	13.62100
Fe XIX	13.63400	Fe XIX	13.63600	Fe XIX	13.64300	Fe XIX	13.64600	Fe XIX	13.64800	Fe XX	13.67000
Fe XIX	13.67200	Fe XIX	13.67300	Fe XXII	13.67400	Fe XIX	13.69100	Fe XIX	13.69400	Fe XXI	13.71700
Fe XIX	13.72000	Fe XIX	13.72100	Fe XIX	13.74100	Fe XIX	13.75400	Fe XIX	13.76200	Fe XIX	13.76900
Fe XXII	13.77100	Ni XIX	13.77800	Fe XX	13.78100	Fe XIX	13.79200	Fe XIX	13.79900	Fe XIX	13.82200
Fe XIX	13.84100	Fe XIX	13.84300	Fe XIX	13.84400	Fe XX	13.84400	Fe XIX	13.87100	Fe XIX	13.87200
Fe XIX	13.93600	Fe XIX	13.93800	Fe XIX	13.94200	Fe XIX	13.95700	Fe XVIII	13.96200	Fe XIX	13.96400
Fe XIX	13.97000	Fe XX	13.97200	Fe XXI	14.00800	Fe XIX	14.01700	Ni XIX	14.04000	Ca XVIII	14.04900
Ca XVIII	14.05900	Fe XIX	14.07100	Fe XIX	14.08600	Fe XIX	14.11400	Fe XX	14.11500	Fe XX	14.12300
Fe XVIII	14.12400	Fe XIX	14.12700	Fe XIX	14.12800	Fe XVIII	14.13600	Fe XVIII	14.14400	Fe XIX	14.17500
Fe XX	14.19000	Fe XVIII	14.20400	Fe XVIII	14.20900	Cr XXI	14.24500	Fe XX	14.24800	Fe XIX	14.25200
Fe XVIII	14.25800	Fe XVIII	14.34400	Fe XVIII	14.35200	V XX	14.35960	Fe XVIII	14.37300	Fe XVIII	14.41900
Fe XVIII	14.45300	Fe XVIII	14.47000	Fe XVIII	14.48700	Fe XX	14.49300	Fe XX	14.50000	Fe XVIII	14.53700
Fe XVIII	14.55100	Fe XIX	14.57000	Fe XVIII	14.58000	Fe XVIII	14.61000	O VIII	14.63430	Fe XIX	14.66400



**Table 2.** (Continued) List of spectral lines in the 1 keV blend. Line intensities vary depending on the shape of the SED,  $\xi$ ,  $N_H$ , and  $T$ .

Ion	$\lambda$ (Å)	Ion	$\lambda$ (Å)	Ion	$\lambda$ (Å)	Ion	$\lambda$ (Å)	Ion	$\lambda$ (Å)	Ion	$\lambda$ (Å)
Fe XIX	14.66900	Fe XVIII	14.67100	Fe XIX	14.69400	Fe XIX	14.73800	Fe XIX	14.74100	Fe XX	14.76400
Fe XVIII	14.77100	O VIII	14.82060	Fe XIX	14.86800	Fe XX	14.91300	Fe XXI	14.91600	Fe XIX	14.93200
Fe XX	14.93200	Fe XIX	14.93500	Ca XVII	14.94000	Fe XIX	14.99200	Fe XVII	15.01300	Fe XIX	15.04200
Fe XX	15.06000	Fe XX	15.06300	Fe XIX	15.08100	Fe XIX	15.11400	Fe XIX	15.16300	O VIII	15.17620
Ar XVI	15.19000	Fe XIX	15.19600	Fe XIX	15.20800	Ti XX	15.21100	Ti XX	15.25300	Fe XVII	15.26200
Fe XIX	15.33000	Fe XIX	15.35200	Fe XX	15.51500	Fe XVIII	15.62200	Fe XVIII	15.76600	Fe XVIII	15.82800
Ti XIX	15.86500	Ar XVI	15.93300	Fe XVIII	16.00500	O VIII	16.00590	Fe XVIII	16.02600	Fe XVIII	16.07200
Fe XIX	16.11000	Fe XIX	16.27200	Fe XIX	16.34000	Ti XVIII	17.31760	Ar XVI	17.73700	Ar XVI	17.74700
Ca XVIII	18.69100	S XIV	18.72000	Ca XVIII	18.73200	O VIII	18.96890	Ca XVII	19.55800	S XIV	19.69000
N VII	19.82580	Ca XVII	20.43400	Ca XVI	20.85900	K XVII	20.89900	N VII	20.90980	K XVII	20.93100
Ca XVI	20.95100	Ca XVI	21.02000	Ca XVI	21.11300	Ca XVI	21.45000	O VII	21.60200	Ca XVI	21.61000
Ca XVI	21.61900	K XVI	21.91100	Ca XV	22.73000	Ca XV	22.73000	Ca XV	22.75900	Ca XV	22.77700
Ca XV	22.82100	S XIV	23.00500	S XIV	23.01500	Ca XVII	23.17500	Ca XVII	23.17500	Ar XVI	23.50600
Ar XVI	23.54600	S XIII	24.59000	Ar XV	24.73700	N VII	24.78100				


**Figure 1.** Variation of the normalized 1 keV emission blend emissivity (dimensionless) with  $\log \xi$  and  $\log N_H$  for PIE plasma in NGC 1313 X-1, NGC 247 ULX-1, Her X-1, Ser X-1, and Cyg X-2. The circular, square, inverted elliptical, and inverted square red data points indicate the best-fit parameters for the PIE emission model for NGC 1313 X-1, NGC 247 ULX-1, Ser X-1, and Cyg X-2, respectively, as discussed in Section 5.

a ratio below 1 suggests a rightward shift. This captures the variation of the centroid shift of the 1 keV emission feature.

#### 4.2 Absorption lines from PIE plasma:

For absorption line generation from PIE plasma, we used target-specific SEDs outlined in Section 3. We examined the variation of  $\text{Abs}_{\text{blend}}$  and  $\text{Abs}_{\text{left}}/\text{Abs}_{\text{right}}$  in response to variations in  $\xi$  and  $N_H$ . We used the same logarithmic grids described earlier in section 4.1 to explore these variations.

In Figure 3, we presented the variation of  $\text{Abs}_{\text{blend}}$  with  $\log \xi$  and  $\log N_H$ . These variations in  $\text{Abs}_{\text{blend}}$  illustrate changes in the strength of the 1 keV absorption feature. When  $\text{Abs}_{\text{blend}}$  approaches 1, it indicates that strong 1 keV absorption residuals are expected, while a value of  $\text{Abs}_{\text{blend}} \ll 1$  suggests weaker absorption residuals.

In Figure 4, we showed the variation of  $\text{Abs}_{\text{left}}/\text{Abs}_{\text{right}}$  with  $\log \xi$  and  $\log N_H$ . This ratio,  $\text{Abs}_{\text{left}}/\text{Abs}_{\text{right}}$ , characterizes the shift in the location of the 1 keV absorption residuals. A ratio exceeding 1 signifies a more pronounced absorption residual to the left of the central emission feature, whereas a ratio below 1 indicates a more

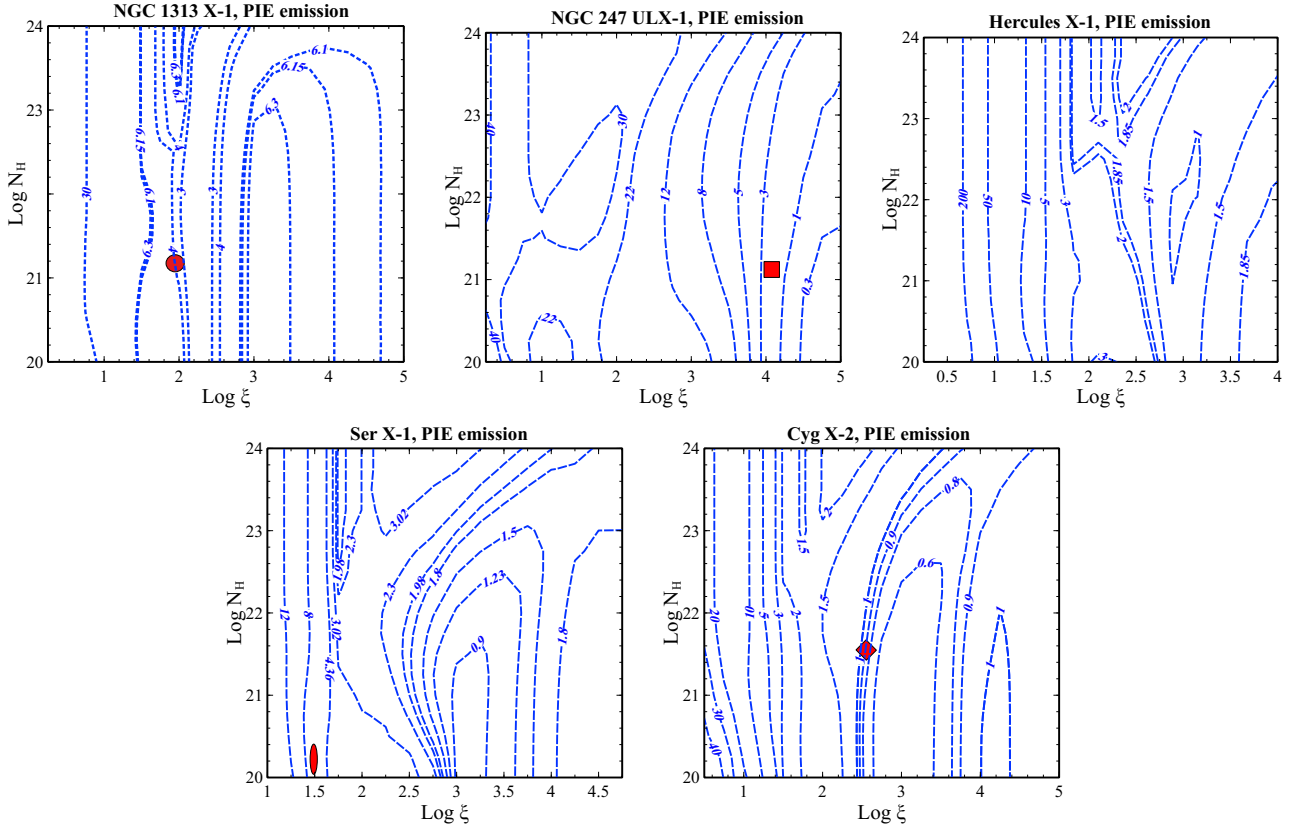


**Figure 2.** Variation of  $E_{\text{m,left}}/E_{\text{m,right}}$  ratio with  $\log \xi$  and  $\log N_{\text{H}}$  for PIE plasma in NGC 1313 X-1, NGC 247 ULX-1, Her X-1, Ser X-1, and Cyg X-2. The circular, square, inverted elliptical, and inverted square red data points indicate the best-fit parameters for the PIE emission model for NGC 1313 X-1, NGC 247 ULX-1, Ser X-1, and Cyg X-2, respectively, as discussed in Section 5.

pronounced dip on the right. This ratio captures the variability in the centroid of the absorption residuals.

### 4.3 Emission lines from CIE plasma:

For studying the emission from a CIE plasma, we investigated the variation in  $E_{\text{m,blend}}$  and  $E_{\text{m,left}}/E_{\text{m,right}}$  with temperature ( $T$ ), and hydrogen column density ( $N_{\text{H}}$ ). A logarithmic grid was created for  $T$  with  $\log T$  values ranging from 6.0 to 8.0, and for  $\log N_{\text{H}}$  with values ranging from 20 to 24, both with increments of 0.1 dex, resulting in a total of 800 grids. For CIE plasma,  $E_{\text{m,blend}}$  and  $E_{\text{m,left}}/E_{\text{m,right}}$  for NGC 247 ULX-1, NGC 1313 X-1, Her X-1, Cyg X-2, and Ser X-1 overlaps as the only difference between emission from these systems stems from different electron density, which gets canceled out while calculating normalized emissivities and emission line ratios. The overlapping contours are displayed with solid red lines.

The left panel of Figure 5 shows the variation of  $E_{\text{m,blend}}$  with  $\log T$  and  $\log N_{\text{H}}$ .  $E_{\text{m,blend}}$  approaches values close to 1 for temperatures around  $\log T \sim 7.0$  and for column densities spanning from  $\log N_{\text{H}} = 20$  to  $\log N_{\text{H}} = 21.5$  when the 1 keV emission feature is the strongest. At higher or lower temperatures, the 1 keV emission feature diminishes in intensity. The right panel of Figure 5 displays the variation of  $E_{\text{m,left}}/E_{\text{m,right}}$  with  $\log T$  and  $\log N_{\text{H}}$ , characterizing the variation in the centroid of the 1 keV emission feature in a CIE plasma. Around  $\log T \sim 7.2$ , the emission feature is centered at 1 keV. For lower temperatures, it shifts to the left, and for higher temperatures, it shifts to the right.

### 4.4 Reflection from accretion disk:

Out of the five XRBs in our sample, Ser X-1 and Cyg X-2 displayed reflection features near 1 keV, prompting us to investigate their variability further. The reflection from the accretion disk has been associated with high column densities (Koljonen & Tomsick 2020), we therefore set  $N_{\text{H}}$  to  $10^{23} \text{ cm}^{-2}$  for the reflection blends. The incident continuum spectral energy distribution (SED)<sup>1</sup> illuminating the accretion disk is derived from the observed SEDs of Ser X-1 and Cyg X-2, after subtracting the diskbb continuum component (see sections 5.4 and 5.5), which represents the contribution from the accretion disk itself. The illuminating SED interacts with the accretion disk, where it is absorbed and subsequently re-emitted, producing characteristic emission lines, including those in the Fe L complex.

For studying the variation in the reflection features, we created a logarithmic grid for  $\xi$ , covering a range of  $\log \xi$  values from 0.5 to 5.0, with increments of 0.1 dex. Figure 6 shows the variation of  $\text{Reflect}_{\text{blend}}$  and  $\text{Reflect}_{\text{left}}/\text{Reflect}_{\text{right}}$  with  $\log \xi$  in Ser X-1 and Cyg X-2. The reflection features are additionally influenced by the viewing angle and inner disk radius, both of which were treated as free parameters, as elaborated in Sections 5.5 and 5.4.

<sup>1</sup> The default settings for reflection modeling in CLOUDY utilize a power-law continuum as the primary radiation source (see the [hazy1](#) manual).

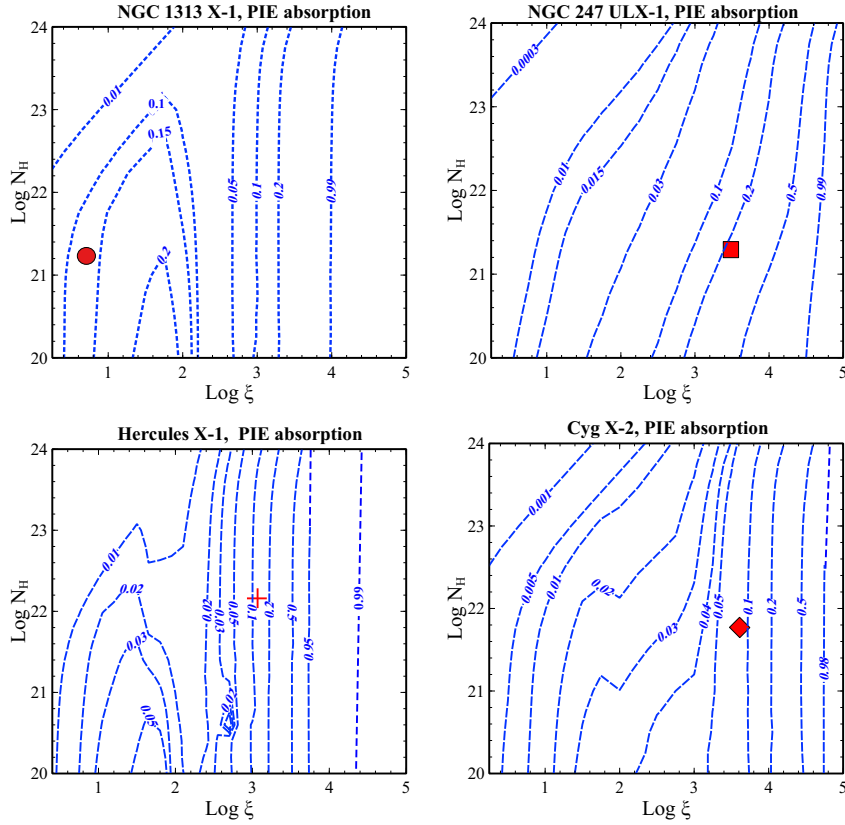


**Figure 3.** Variation of the normalized 1 keV absorption blend emissivity with  $\log \xi$  and  $\log N_H$  for PIE plasma in NGC 1313 X-1, NGC 247 ULX-1, Her X-1, and Cyg X-2. Given the absence of an accretion wind associated with Serpens X-1, we have refrained from examining the absorption PIE features for Serpens X-1. The red circle, square, cross, and inverted square data points represent the best-fit parameters for NGC 1313 X-1, NGC 247 ULX-1, Her X-1, and Cyg X-2, respectively, for the PIE absorption model detailed in Section 5.

## 5 FITTING THE 1 KEV FEATURES WITH CLOUDY

We performed spectral fitting in XSPEC version 12.01 (Arnaud 1996). The SEDs of the respective XRBs were incorporated into CLOUDY for spectral modeling of the PIE emission/absorption and reflection features. To model the PIE line emission/absorption for both targets, we utilized logarithmic grids for two key parameters:  $\xi$ , which ranged from 0 to 5 in increments of 0.1, and  $N_H$ , which spanned from 20 to 24 in increments of 0.1. For the CIE line emission, we ran logarithmic grids on temperature ( $T$ ), ranging from 6 to 8 in increments of 0.1, and on  $N_H$ , which spanned from 20 to 24 in increments of 0.1. To model the reflection lines, we utilized a logarithmic grid for  $\xi$ , ranging from 0 to 5 in increments of 0.1, a logarithmic grid for inner radius ( $r$ ) spanning from 6 to 8 in increments of 0.1, a linear grid for the inclination angle ranging from 0 to 90 degrees in increments of 5 degrees, and kept the hydrogen column density fixed at  $N_H = 10^{23} \text{ cm}^{-2}$ . The electron density was systematically varied using logarithmic grids, ranging from  $\log(n_e)=10$  to  $\log(n_e)=20$  with steps of 0.1 for all three cases mentioned above. Subsequently, we converted these files into FITS formats compatible with XSPEC. These XSPEC-readable files were then utilized in our spectral fitting analyses. CLOUDY fittings also calculate velocity broadening, and the resulting broadening values are presented for all systems in this section for both the CIE and PIE models. The best-fit parameters were determined by minimizing the C-statistics (Cash 1979).

### 5.1 NGC 1313 X-1:

In our initial analysis, we aimed to fit the observed spectrum of NGC 1313 X-1 using a two-blackbody continuum model, specifically, `tbabs*(bbody+bbbody)` in the 0.5–2.0 keV energy band. The `tbabs` model was employed to account for Galactic absorption, with the absorbing hydrogen column density set at  $7 \times 10^{20} \text{ cm}^{-2}$  (HI4PI Collaboration et al. 2016)<sup>2</sup>. We found the best-fit temperature of  $0.35 \pm 0.02 \text{ keV}$  for the lower-energy blackbody component and of  $1.55 \pm 0.03 \text{ keV}$  for the higher-energy blackbody component. Figure 8, Panel a, displays the best-fitted two-blackbody continuum model along with the observed spectra of NGC 1313 X-1 in the 0.5–2 keV energy band. The sub-figures at the bottom of each panel in Figure 8 show the residual of the observed spectra after fitting, which estimated as  $(\text{data} - \text{model})/\text{error}$ . Notably, we observed a significant emission residual within the energy range of 0.6 to 1.25 keV. This emission residual displayed a leftward shift from 1 keV, primarily concentrating in the 0.6 to 1.0 keV energy range. Furthermore, the absorption residuals were more prominent in the 0.5 to 0.8 keV energy range, with fainter residuals observed for energies above 1 keV.

Following that, we adopted a spectral-fitting approach that combined the two-blackbody continuum model with a CIE plasma emission model, as illustrated in Panel b of Figure 8. The fitting process resulted in the best-fit temperature for the CIE emission model, yielding  $\log(T/\text{keV}) = 7.1 \pm 0.1$ , along with a best-fit column density of

<sup>2</sup> <https://heasarc.gsfc.nasa.gov/cgi-bin/Tools/w3nh/w3nh.pl>

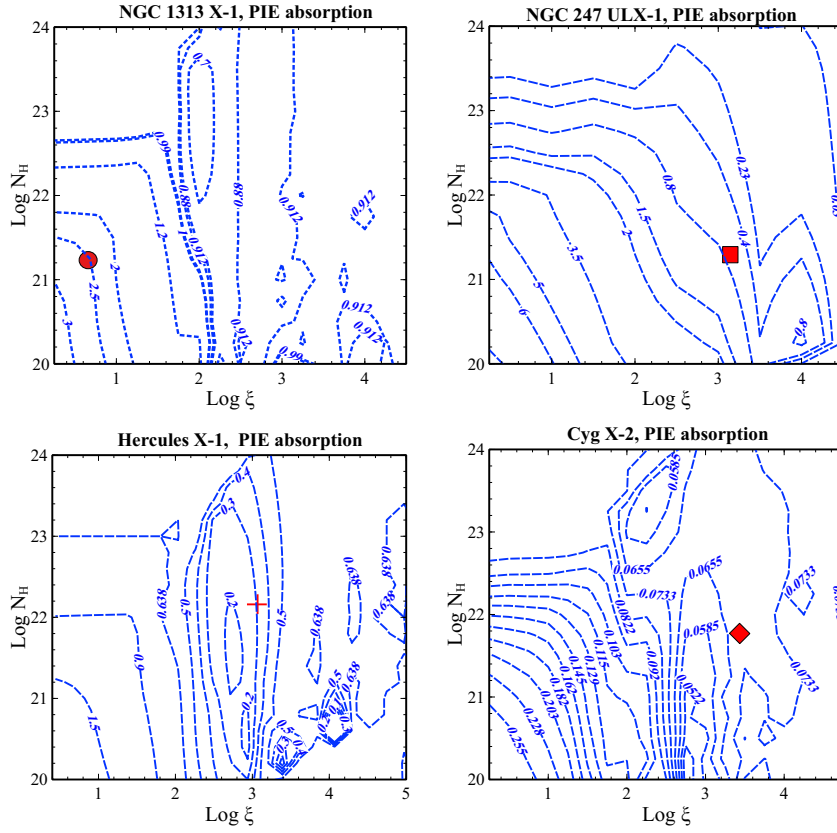


**Figure 4.** Variation of  $\text{Abs}_{\text{left}}/\text{Abs}_{\text{right}}$  ratio with  $\log \xi$  and  $\log N_{\text{H}}$  for PIE plasma in NGC 1313 X-1, NGC 247 ULX-1, Her X-1, and Cyg X-2. Given the absence of an accretion wind associated with Serpens X-1, we have refrained from examining the absorption PIE features for Serpens X-1. The red circle, square, cross, and inverted square data points represent the best-fit parameters for NGC 1313 X-1, NGC 247 ULX-1, Her X-1, and Cyg X-2, respectively, for the PIE absorption model detailed in Section 5.

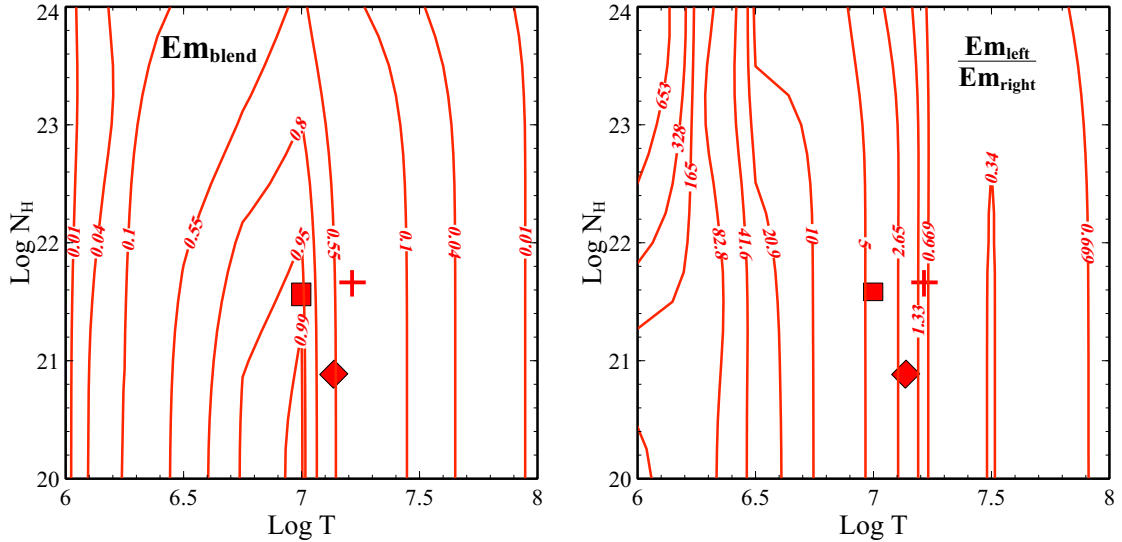


**Figure 5.** Left panel: Variation of the normalized 1 keV emission line blend emissivity in CIE plasma. Right panel: Variation of  $\text{Em}_{\text{left}}/\text{Em}_{\text{right}}$  ratio with  $\log T$  and  $\log N_{\text{H}}$  for CIE plasma. The red square, cross, and inverted square data points represent the best-fit parameters for NGC 247 ULX-1, Her X-1, and Cyg X-2, respectively, for the CIE emission model detailed in Section 5.



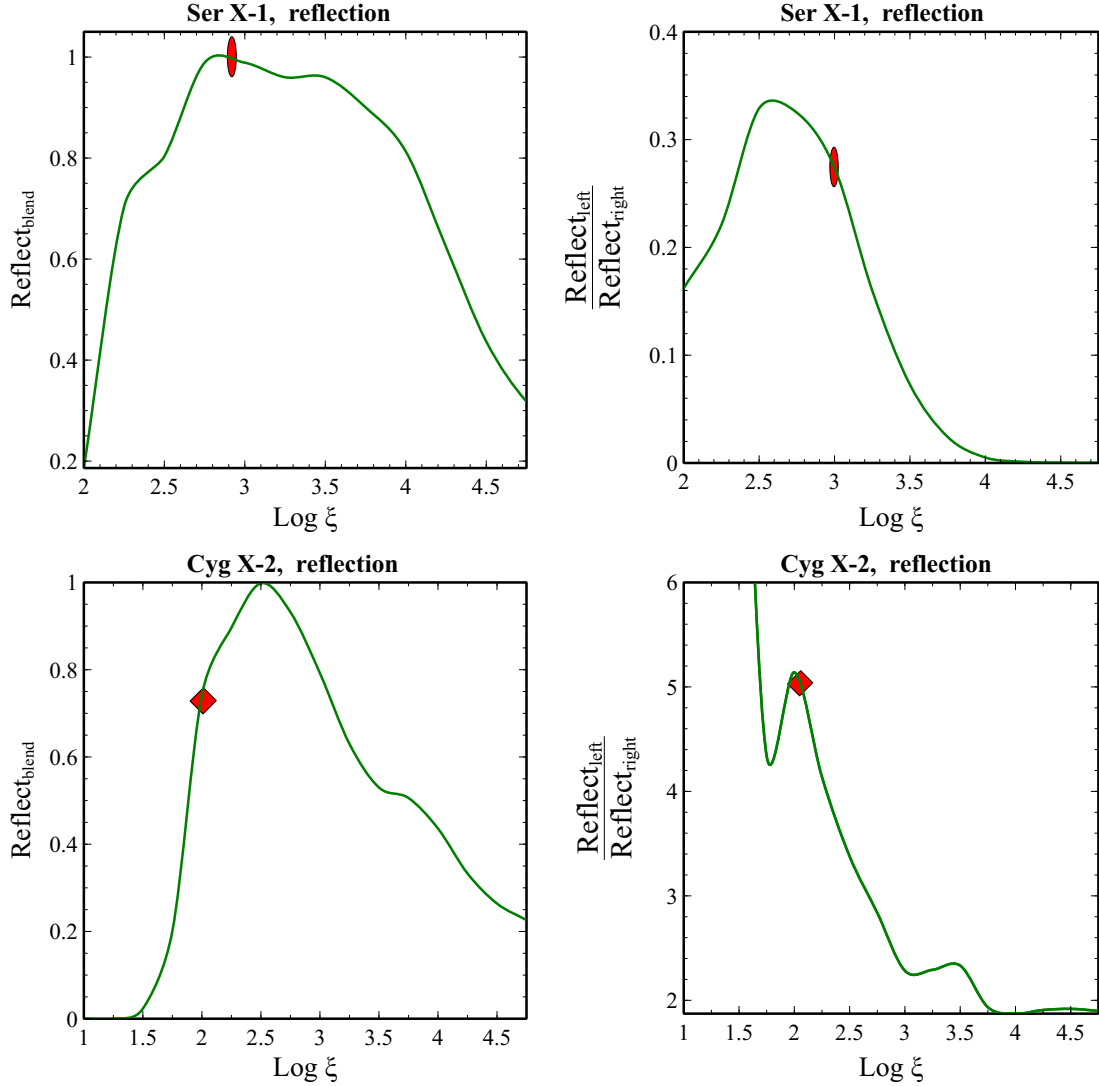


**Figure 6.** Left panels: Variation of the Reflect<sub>blend</sub> with log  $\xi$  for Ser X-1 and Cyg X-2. Right panels: Variation of Reflect<sub>left</sub>/Reflect<sub>right</sub> ratio with log  $\xi$  for Ser X-1 and Cyg X-2. The vertical elliptical and inverted square data points represent the best-fit log  $\xi$  values for Ser X-1 and Cyg X-2 as detailed in Section 5.

$\log(N_{\text{H}}/\text{cm}^2) = 21.0 \pm 0.1$ . The blackbody temperatures remained unchanged. The best-fit electron density was determined to be  $\log(n_e/\text{cm}^{-3}) = 10.2 \pm 0.1$ . Although adding the CIE model with the blackbody continuum improved the overall fit to the observed spectra slightly with  $\Delta\text{C-stat} > 30$ , there was not a substantial improvement in fitting the residuals. Notably, the strong O VIII line at  $\sim 0.65$  keV remained challenging to fit adequately. This simulation did not yield a significantly stronger O VIII emission feature in comparison to the lines in the vicinity of 1 keV. Given the presence of a stronger O VIII emission feature in NGC 1313 X-1, particularly in contrast to the lines around 1 keV, it is evident that relying solely on the CIE emission line feature is inadequate for modeling the 1 keV blend emission in NGC 1313 X-1.

Next, we attempted to model the 1 keV feature by combining the two-blackbody continuum model with a PIE plasma emission/absorption model, as depicted in Panel c of Figure 8. We adjusted the absorption model for NGC 1313 X-1 to include a blueshift of  $0.07c$ , based on previous observations that linked the absorption residuals to a slower wind component in the intermediate-bright state (Pinto et al. 2020). The blackbody temperatures were determined to

be  $0.36 \pm 0.03$  and  $1.55 \pm 0.04$  keV, respectively. This combined model provided a good fit for both the 1 keV emission blend, which includes the prominent O VIII emission feature, as well as the absorption dips with  $\Delta\text{C-stat} > 80$  compared to the two-blackbody model. The best-fit parameters for the PIE emission model were found to be  $\log \xi = 1.93 \pm 0.05$ , accompanied by a best-fit column density of  $\log(N_{\text{H}}/\text{cm}^2) = 21.1 \pm 0.1$ . Additionally, the best-fit parameters for the PIE absorption model were  $\log \xi = 0.7 \pm 0.1$ , and  $\log(N_{\text{H}}/\text{cm}^2) = 21.2 \pm 0.1$ . The line broadening measured at  $\sim 3000$  km/s. In Figures 1, 2, 3, and 4, the values of the best-fit parameters of the two-blackbody+PIE absorption/emission models are highlighted using red circles on the contour plots.

## 5.2 NGC 247 ULX-1:

Our initial analysis aimed to fit the observed spectrum of NGC 247 ULX-1 within the energy band of 0.5–2.0 keV. To achieve this, we utilized a two-blackbody continuum model:  $\text{tbabs}^*(\text{bbody}+\text{bbody})$ . Within this model,  $\text{tbabs}$  was used to account for Galactic absorption, with the absorbing hydrogen column density fixed at  $6 \times 10^{20}$

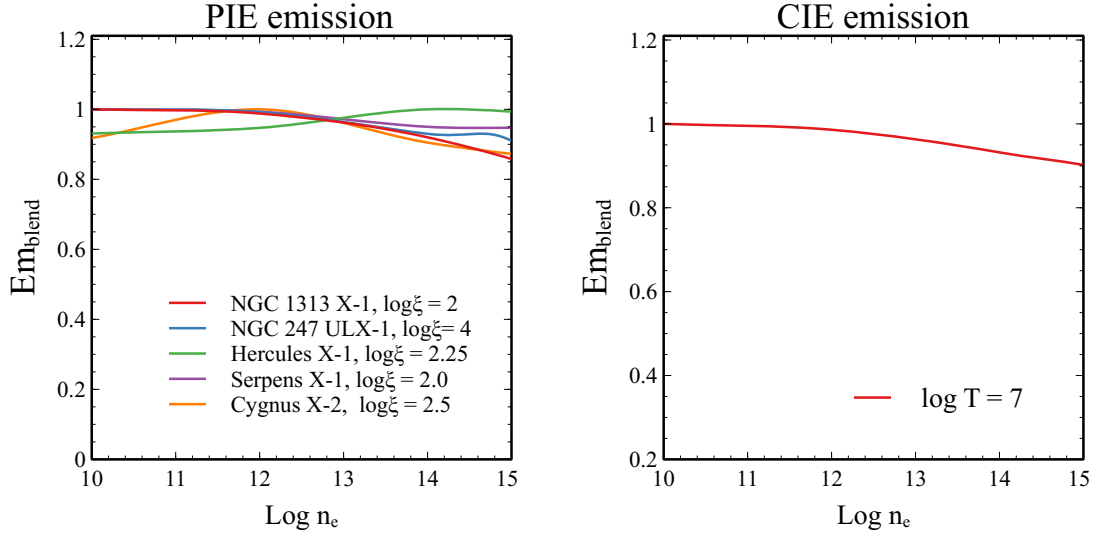


**Figure 7.** Left panel: Variation of the normalized 1 keV emission line blend emissivity in PIE plasma with  $\log n_e$  at the value of  $\log \xi$  where the line blend emissivity reaches its maximum strength. Right panel: Variation of the normalized 1 keV emission line blend emissivity in CIE plasma with  $\log n_e$  at the value of  $\log T$  where the line blend emissivity reaches its maximum strength.

$cm^2$  (HI4PI Collaboration et al. 2016). Our analysis yielded the best-fit temperatures of  $0.14 \pm 0.01$  keV for the lower-energy blackbody component and  $0.44 \pm 0.02$  keV for the higher-energy blackbody component. Figure 9, Panel a, shows the best-fitted two-blackbody continuum model overlaid with the observed spectra of NGC 247 ULX-1 within the 0.5–2 keV energy range. The corresponding residual is displayed in the bottom sub-figure of the panel. Significant emission residuals were observed within the energy range of 0.8 to 1.1 keV. These emission residuals displayed a leftward shift from 1 keV and primarily concentrating between 0.8 and 1.0 keV. In addition, significant absorption residuals were identified in two distinct energy intervals: between 0.55 to 0.85 keV and 1.1 to 1.5 keV. Notably, the absorption residuals in the latter energy range exhibited a more pronounced absorption dip.

Next, we combined the two-blackbody continuum model with a CIE plasma emission model in our spectral analysis, as displayed in Panel b of Figure 9. The blackbody temperatures remained unchanged. The fitting process yielded a best-fit temperature of  $\log(T/\text{keV}) = 6.99 \pm 0.02$ , along with a best-fit column density of  $\log(N_H/\text{cm}^2) = 21.5 \pm 0.1$ . The best-fit electron density was  $\log(n_e/\text{cm}^{-3}) = 11.4 \pm 0.1$ . This modified model marginally improved the fit with a  $\Delta C\text{-stat} > 60$  compared to the two-blackbody model. The inclusion of the CIE emission component effectively resolved the emission residuals, eliminating them (refer to the bottom subfigure in Panel b). However, the absorption residuals persisted in the spectrum.

Following that, we aimed to model the 1 keV feature by merging the two-blackbody continuum model with a PIE plasma emission/absorption model, as illustrated in panel c of Figure 9. We adjusted the absorption model for NGC 247 ULX-1 to include a blueshift of 0.17c, reflecting the previously observed absorption residuals linked to a strong outflow (Pinto et al. 2021). The fitting showed further improvement compared to both the two-blackbody and two-blackbody+CIE emission models, resulting in  $\Delta C\text{-stat} > 80$  compared to the continuum-only fit. The fitting process resulted in a best-fit ionization parameter of  $\log \xi = 4.1 \pm 0.1$  and a best-fit column density of  $\log(N_H/\text{cm}^2) = 21.0 \pm 0.1$  for the emission lines and  $\log \xi = 3.4 \pm 0.1$  and a best-fit column density of  $\log(N_H/\text{cm}^2) = 21.7 \pm$

0.1 for the absorption lines. The blackbody temperatures remained unchanged. The best-fit electron density was  $\log n_e = 11.4 \pm 0.1$  for the emission component and  $\log(n_e/\text{cm}^{-3}) = 13.7 \pm 0.1$  for the absorption component. The two-blackbody+PIE emission/absorption model effectively fit the absorption dips but did not provide a good fit for the emission features. The robust fit of the absorption feature by the two-blackbody+PIE model strongly indicates its origin in the PIE plasma. Furthermore, the effective fit of the emission feature with the two-blackbody+CIE emission model implies that the emission predominantly arises from the CIE plasma.

Finally, to effectively model both the absorption and emission features, we used a two-blackbody+CIE emission+PIE emission/absorption plasma model to fit the observed spectrum, as shown in panel d of Figure 9, obtaining a  $\Delta C\text{-stat} > 110$  compared to the continuum-only fit. The best-fit temperatures were determined to be  $0.15 \pm 0.02$  keV and  $0.44 \pm 0.04$  keV. The best-fit parameters for the CIE model were  $\log(T/\text{keV}) = 7.00 \pm 0.02$  and  $\log(N_H/\text{cm}^2) = 21.5 \pm 0.1$ . For the PIE emission model, the best-fit parameters were  $\log \xi = 4.1 \pm 0.1$  and  $N_H = 21.0 \pm 0.1$ , while for the PIE absorption model, the best-fit parameters were  $\log \xi = 3.5 \pm 0.1$  and  $\log(N_H/\text{cm}^2) = 21.3 \pm 0.1$ . We found the line broadening to be  $\sim 1500$  km/s. The best-fit electron densities were identical to that of the CIE emission and PIE emission/absorption models, as detailed in the preceding two paragraphs. Both emission and absorption residuals were effectively eliminated, as evident in the bottom subfigure of panel d. In Figures 1, 2, 3, 4, and 5, the values of the best-fit parameters for the two-blackbody+CIE emission+PIE emission/absorption plasma model are indicated by red squares on the contour plots.

### 5.3 Hercules X-1:

We initially fitted the spectrum in the 0.56–1.6 keV energy band using the XSPEC model `tbabs*(bbody+powerlaw)`, with the Galactic absorption hydrogen column density fixed at  $1.5 \times 10^{20} \text{ cm}^2$  (HI4PI Collaboration et al. 2016). The best-fit temperatures obtained for the blackbody was  $0.05 \pm 0.01$  keV and the powerlaw index was  $1.992 \pm$

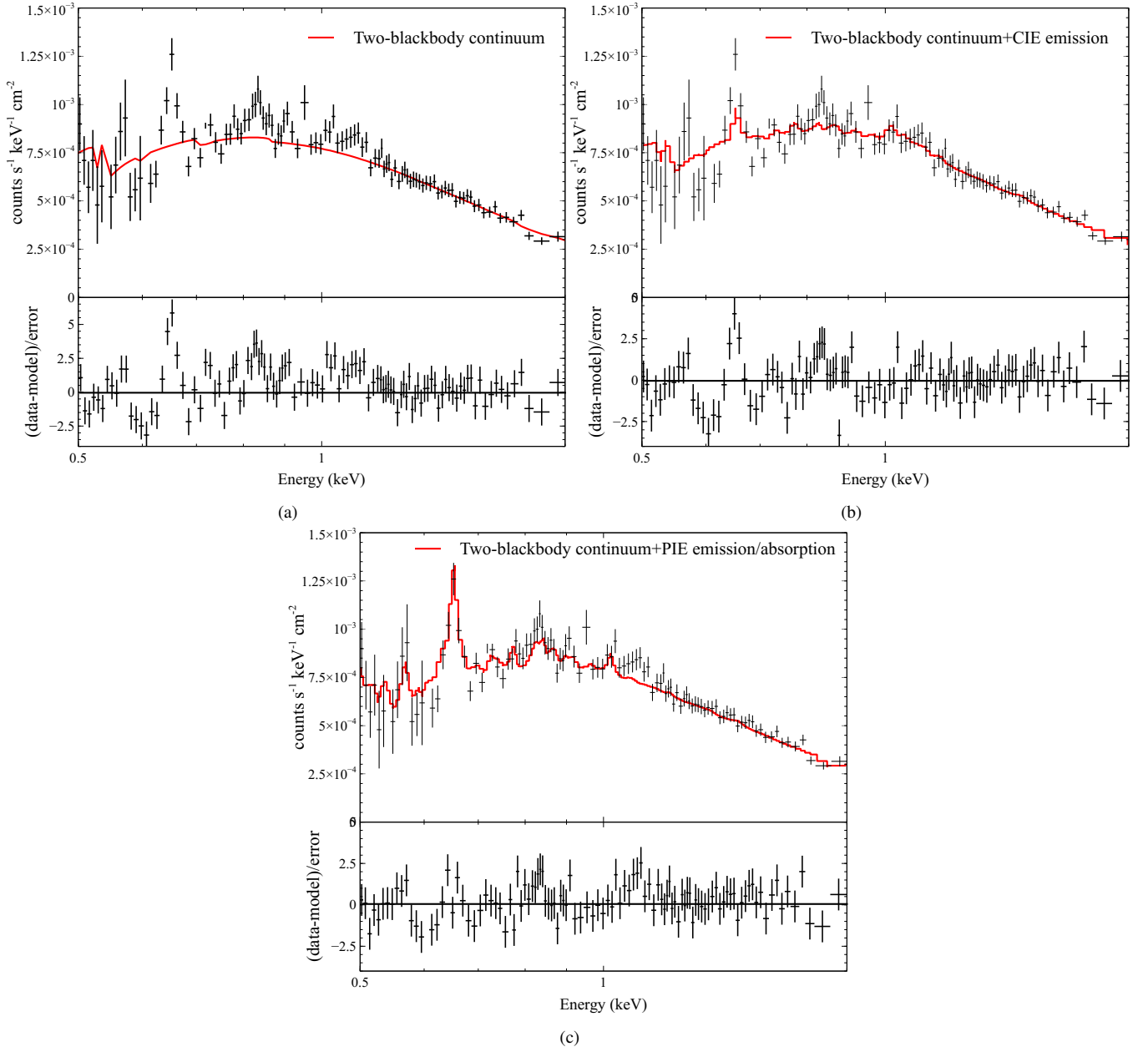


**Figure 8.** a) Combined first-order spectra of NGC 1313 X-1, overplotted with best-fitting two blackbody continuum model, the 1 keV residual is visible within 0.6 and 1.25 keV. b) Spectra of NGC 1313 X-1 overlaid with the continuum model + line emission from CIE plasma, with the 1 keV emission/absorption residuals persisting. c) The same spectra overlaid with continuum model+ PIE line emission, effectively resolving the 1 keV emission/absorption residuals.

0.003 keV. Figure 10, Panel a, illustrates the overlaid best-fitted continuum model and observed spectra of Hercules X-1 in the 0.56–1.6 keV energy range. The residual, shown in the lower sub-figure, reveals significant emissions between 0.8 and 1.18 keV, concentrated mainly between 0.8 and 1.0 keV, and for energies higher than 1.6 keV. Absorption residuals were found in two distinct energy intervals: 0.5 to 0.8 keV and 1.2 to 1.6 keV.

Following this, we integrated the continuum model with a CIE plasma emission model in our spectral analysis, as illustrated in panel b of Figure 10. For the CIE component, we obtained a best-fit temperature of  $\log(T/\text{keV}) = 7.2 \pm 0.1$ , a best-fit column density of  $\log(N_{\text{H}}/\text{cm}^2) = 21.6 \pm 0.1$ , and a best-fit electron density of  $\log(n_e/\text{cm}^{-3}) = 10.6 \pm 0.1$  (The best-fit blackbody temperatures remained unchanged).

While the inclusion of the CIE emission component notably diminished the emission residuals between 0.8 and 1.18 keV, substantial residuals persisted above 1.2 keV, and some remained below 0.8 keV, as shown in the bottom subfigure in panel b. The best-fit velocity of the CIE emission lines were found to be  $\sim 900$  km/s. The addition of a CIE model significantly improved the fit quality ( $\Delta\text{C-stat} > 170$ ). Subsequently, we tried to model the residuals by combining the continuum model with a PIE plasma emission/absorption model, as depicted in panel c of Figure 10. The PIE component required incorporating plasma with multiple velocities, resulting in a narrow O VII emission line at 0.57 keV with a velocity width  $\sim 1200$  km/s and a broad O VIII emission line at 0.65 keV with a velocity width of  $\sim 6000$  km/s. Additionally, there were slightly blueshifted ( $\sim 0.003c$ )

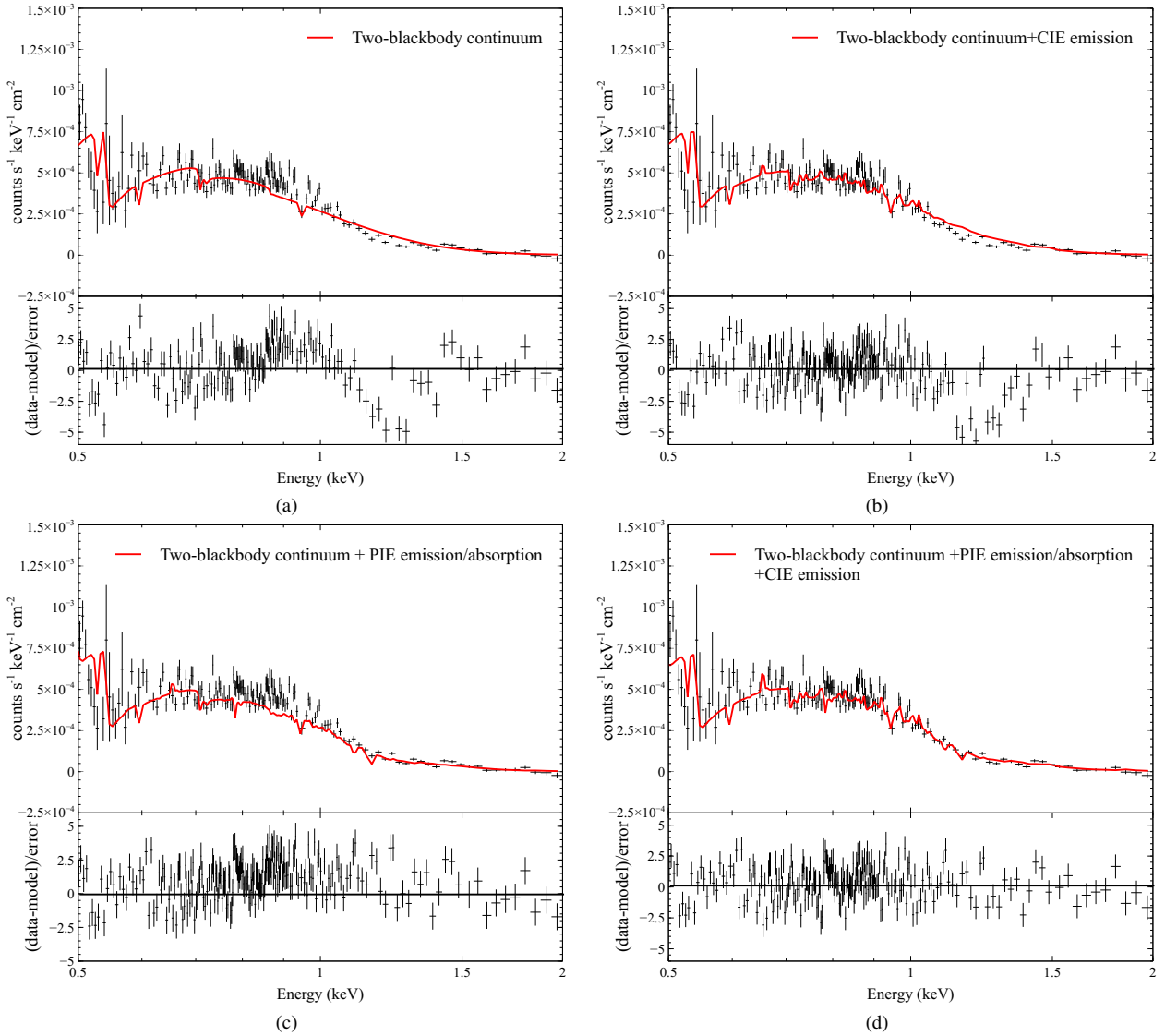


**Figure 9.** a) Combined first-order spectra of NGC 247 ULX-1, overlaid with best-fitting two blackbody continuum model, the 1 keV residual is visible. b) NGC 247 ULX-1 spectra, featuring the continuum model with line emission derived from a CIE model, successfully accounting for the 1 keV emission residual, while the 1 keV absorption residual remains. c) Same spectra of NGC 247 ULX-1, overlaid with the continuum model along with line emission/absorption produced by a PIE model, effectively addressing the 1 keV absorption residual while the 1 keV emission residual persists. d) Spectra of NGC 247 ULX-1 overlaid with combined PIE and CIE emission/absorption models along with the continuum model, comprehensively accounting for the 1 keV emission/absorption feature.

absorption lines with a velocity width of  $\sim 1250$  km/s. The blackbody temperatures remained unchanged, for the narrow emission line at  $\log \xi = 1.11 \pm 0.01$  and  $\log(N_{\text{H}}/\text{cm}^2) = 21.6 \pm 0.1$ , the broad emission line at  $\log \xi = 1.80 \pm 0.01$  and  $\log(N_{\text{H}}/\text{cm}^2) = 22.1 \pm 0.1$ , other emission line blend around 1 keV at  $\log \xi = 2.6 \pm 0.02$  and  $\log(N_{\text{H}}/\text{cm}^2) = 21.4 \pm 0.1$ , absorption lines at  $\log \xi = 3.00 \pm 0.02$ , and  $\log(N_{\text{H}}/\text{cm}^2) = 22.1 \pm 0.1$ , and electron density at  $\log(n_{\text{e}}/\text{cm}^{-3}) = 10.5 \pm 0.1$ . Despite substantial improvement in the residuals below 0.8 keV, significant residuals remained between 0.8 and 1.6 keV, as indicated in the bottom sub-panel of Figure 10 c. The inclusion of a PIE model improved the fit quality compared to the continuum model ( $\Delta\text{C-stat} > 80$ ) but was inferior to the fit achieved with the continuum+CIE model.

In our final approach to model both absorption and emission features comprehensively, we used a continuum+CIE emission+PIE emission/absorption plasma model, as displayed in Figure 10d. All residuals within the range of 0.56 - 1.6 keV were successfully eliminated

including the emission/absorption 1 keV residual with  $\Delta\text{C-stat} > 270$  compared to the continuum-only model (see the bottom sub-panel of Figure 10 d). The best-fit hydrogen column density was determined to be  $\log(N_{\text{H}}/\text{cm}^2)$  of  $21.6 \pm 0.1$  for the CIE plasma,  $\log(N_{\text{H}}/\text{cm}^2) = 22.1 \pm 0.1$  for the PIE plasma, and the electron density was  $\log(n_{\text{e}}/\text{cm}^{-3}) = 10.7 \pm 0.05$  for both CIE and PIE plasma. The blackbody temperature, power-law index, ionization parameter values for the PIE plasma, temperature for the CIE plasma, and all the velocity widths remained unchanged. The best-fit parameters of this final model are symbolized by red crosses in the contour plots shown in Fig 3, 4, and 5. Due to the multiple components of PIE emission for  $\xi$  and  $N_{\text{H}}$ , it was not feasible to mark the PIE emission contour plots with a single data point for the best-fit parameter.

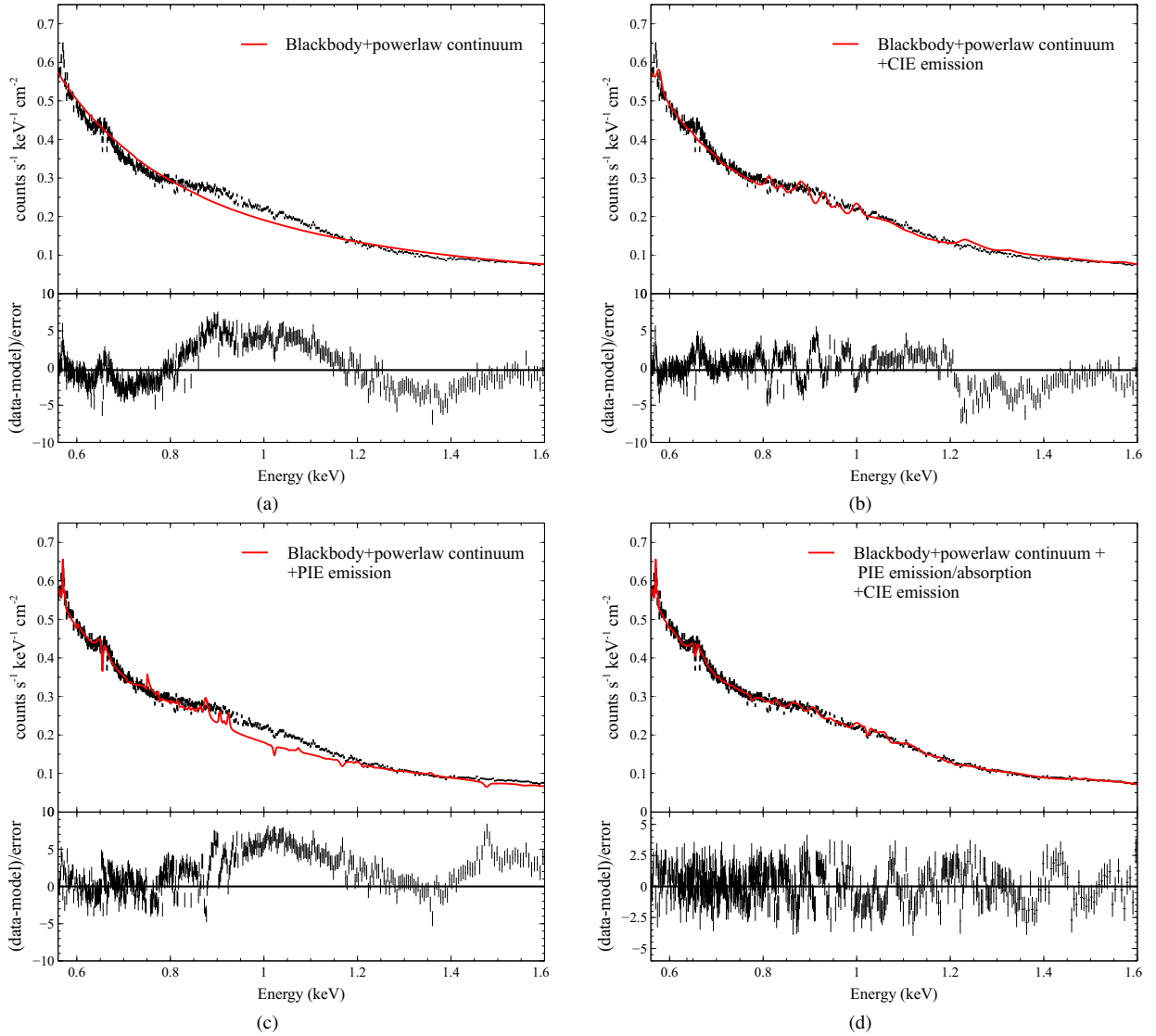


**Figure 10.** a) Combined first-order spectrum of Hercules X-1, overlaid with best-fitting blackbody+powerlaw continuum model, the 1 keV residual is visible. b) Adding CIE emission to the continuum model significantly improves the emission residuals between 0.8-1.2 keV, while the absorption residual remains. c) The continuum model along with line emission/absorption produced by a PIE model improves the fit below 0.8 keV, but significant emission/absorption residuals persist for energies  $> 0.8$  keV. d) The combination of the continuum, CIE emission, and PIE emission/absorption models successfully eliminated most of the residuals across all energies between 0.56 and 1.6 keV.

#### 5.4 Serpens X-1

The continuum in Ser X-1 has been previously characterized using a blend of a disk blackbody component, a single-temperature blackbody component, and a power-law component for a broadband fit using *NuSTAR* and *NICER* observations (Miller et al. 2013; Ludlam et al. 2018). In the narrower 0.5-2.0 keV energy range, our analysis revealed that a basic combination of a blackbody and disk blackbody was sufficient for fitting the continuum, with the introduction of a power law showing no improvement in the fit. We therefore proceeded with the model `tbabs*(diskbb+bbbody)`, with the Galactic absorption hydrogen column density set at  $\sim 4.4 \times 10^{21} \text{ cm}^{-2}$  (HI4PI Collaboration et al. 2016) for fitting the continuum in Ser X-1. The best-fit temperature for the `diskbb` component was  $1.05 \pm 0.05$  keV, while the `bbbody` component had a best-fit temperature of  $1.90 \pm 0.06$  keV. Figure 11, Panel a, shows the continuum model overlaid on the spectrum, while the lower sub-figure shows a significant emission

residual in the 0.65-0.9 keV range, and a less pronounced emission residual in the 0.9-1.3 keV range.

Following that, we integrated a PIE plasma emission model into our spectral analysis, utilizing the SED described in Section 3.3, and combining it with the continuum model to form a continuum+PIE model, as illustrated in panel b of Figure 11. The best fit parameters were determined to be  $\log \xi = 1.5 \pm 0.1$ ,  $\log(N_{\text{H}}/\text{cm}^2) = 20.2 \pm 0.2$ , and  $\log(n_e/\text{cm}^{-3}) = 10.1 \pm 0.1$ . The best-fit temperatures for the continuum models remained unaltered. The measured widths of the PIE emission lines were found to be  $\sim 4200$  km/s. The addition of the PIE model successfully eliminated the residuals within the 0.65-0.9 keV range, although the residual in the 0.9-1.3 keV range persisted (see the lower sub-figure of panel b, Figure 11). The fit quality significantly improved compared to the continuum-only fit ( $\Delta\text{C-stat} > 2000$ ).

When hard X-rays from an external source interact with an accretion disk, one can anticipate the occurrence of disk reflection. In earlier



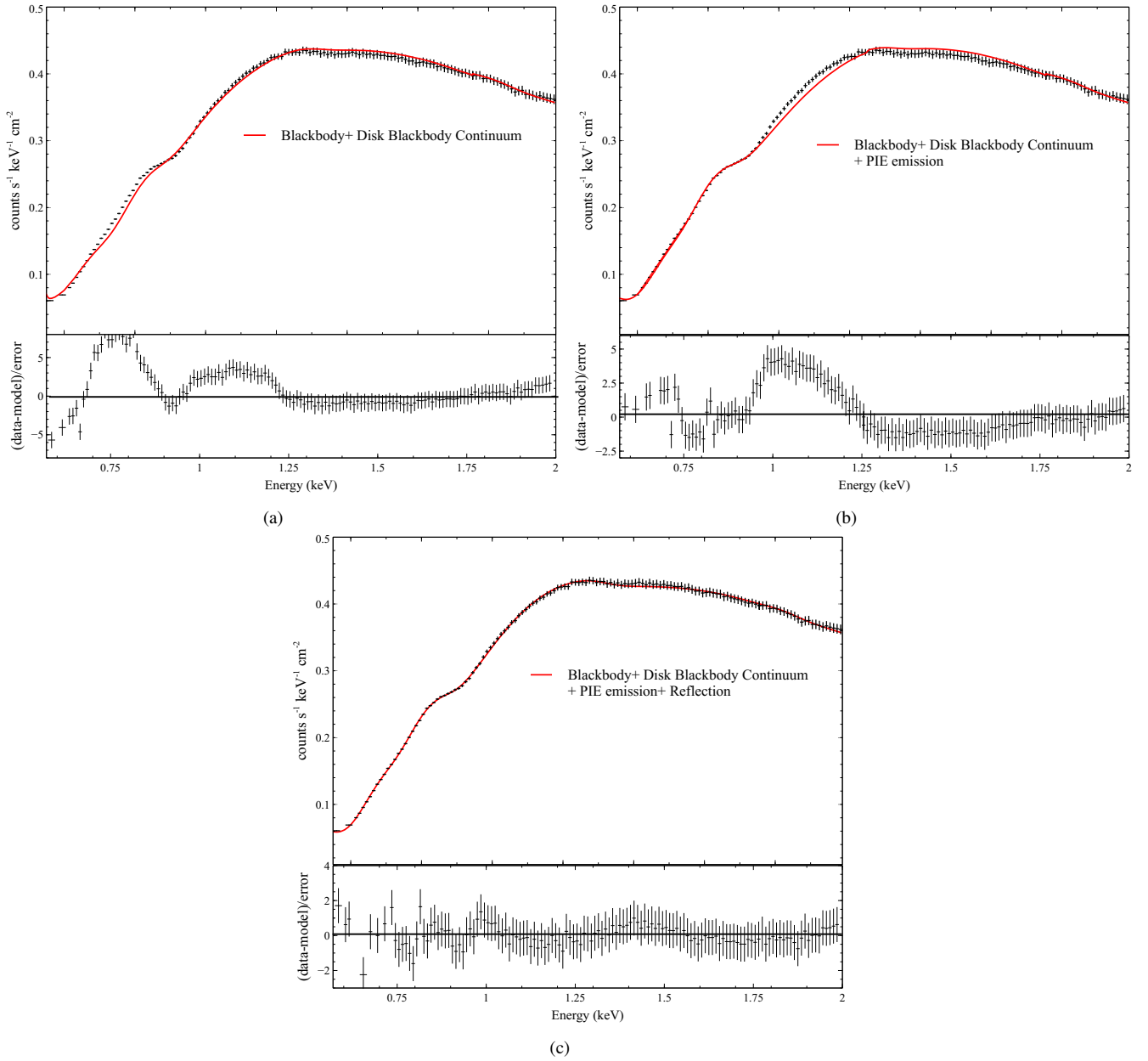


**Figure 11.** a) *NICER* spectrum of Ser X-1, overlaid with best-fitting continuum model, a more pronounced emission residual is found (0.5-0.9 keV) with a less pronounced emission residual (0.9-1.3 keV). b) The same spectrum overlaid with the continuum model + line emission from PIE plasma. The residual between 0.5-0.9 keV have largely diminished, while the residual between 0.9-1.3 keV persists. c) The same spectrum overlaid with continuum model+ PIE line emission+ reflection emission effectively resolving both emission residuals.

investigations, reflection features were identified in Ser X-1, including both Fe-K and Fe-L features (Miller et al. 2013; Ludlam et al. 2018; Mondal et al. 2020). To address both emission residuals, we incorporated a continuum+PIE+reflection model for modeling the spectrum, as displayed in panel c of Figure 11. The reflection feature was self-consistently modeled with *CLOUDY* (see appendix for model details) with the SED described in Section 3.3. The electron density was set at  $\log(n_e/\text{cm}^{-3}) = 20$ , and  $\log(N_H/\text{cm}^2)$  was set at 23.0 since previous reflection models have assumed high electron density and column density (Jiang et al. 2019). The best-fit parameters were determined to be  $\log \xi = 3.2 \pm 0.1$ , an inner radius of  $\log(r_{in}/\text{cm}) = 6.20 \pm 0.15$ , and an illumination angle of  $29^\circ \pm 5^\circ$ . The blackbody temperatures in the continuum model remained unchanged. The fit

quality further improved compared to the continuum-only model, with a  $\Delta\text{C-stat} > 2900$ . Both emission residuals were successfully eliminated, as demonstrated in the lower subfigure of panel c, Figure 11. The contour plots presented in Fig 1, 2 and the linear plot showcased in Fig 6 depict the best-fit parameters of this final model, symbolized by red vertical ellipses.

### 5.5 Cyg X-2:

To model the continuum emission in Cyg X-2 within the energy range of 0.5-2.0 keV, we utilized the XSPEC model *tbabs\*(diskbb+powerlaw)*, with the Galactic absorption hydrogen column density fixed at  $2.2 \times 10^{21} \text{ cm}^2$ . Although broader energy

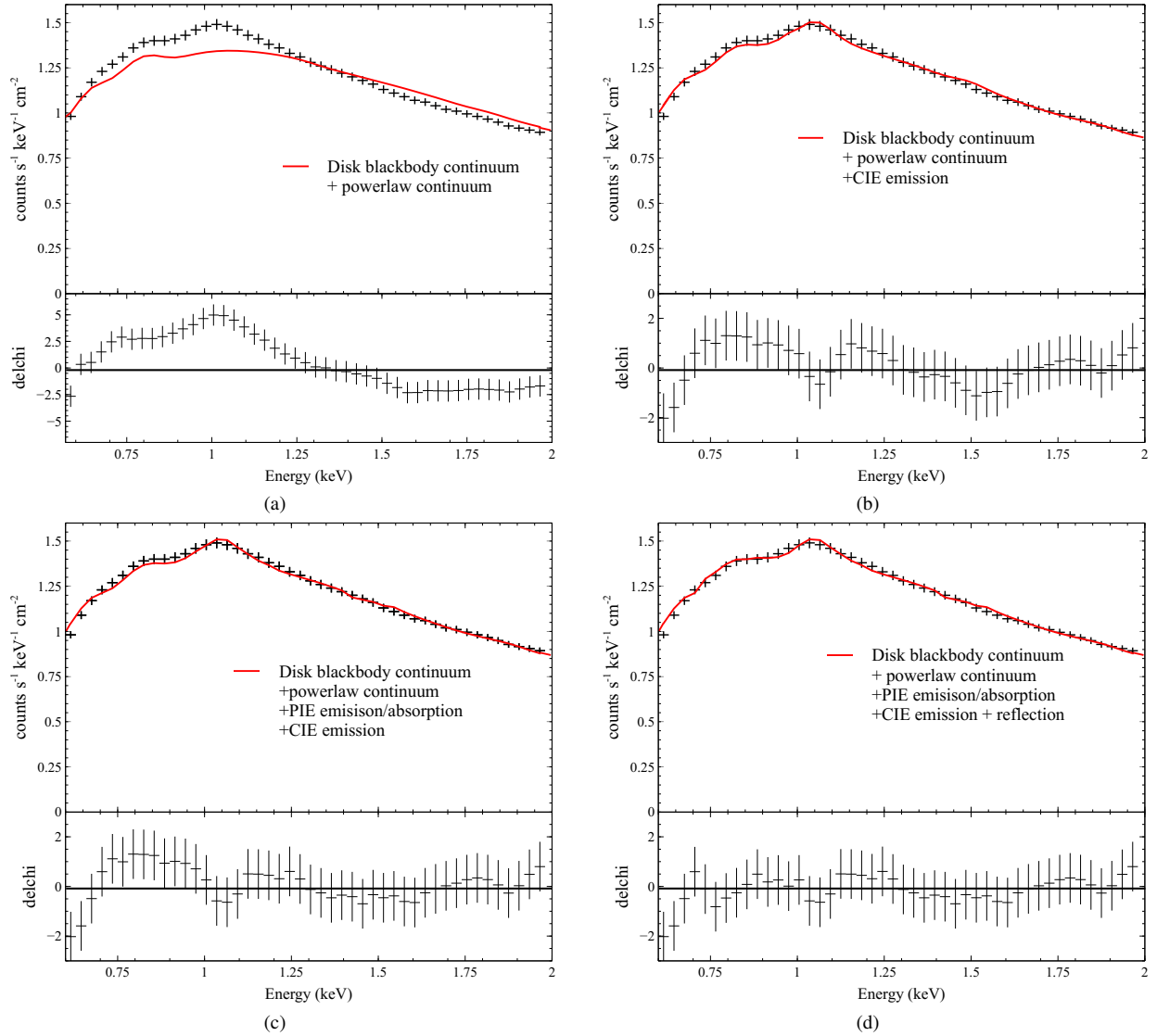


**Figure 12.** a) *NICER* spectrum of Cyg X-2, overlaid with best-fitting continuum model, the 1 keV residual is more prominent in emission, less noticeable in absorption. b) Adding CIE emission to the continuum model significantly improves the residuals, although some emission residuals persist in specific energy ranges (0.65-1 keV and 1.1-1.2 keV), with minor absorption residuals in the 1.4-1.6 keV range. c) The continuum + CIE emission + PIE emission/absorption effectively eliminates all the absorption residuals, small emission residual remains between 0.65-1.0 keV. d) The continuum + CIE emission + PIE emission/absorption+ reflection model eliminates all the emission and absorption residuals.

spectra would require an additional single-temperature blackbody component (Ludlam et al. 2022), our continuum model adequately fits the 0.5-2.0 keV range. The best-fit temperature for the *diskbb* component was found to be  $1.64 \pm 0.03$  keV, with a photon index for the power-law measured at  $2.78^{+0.06}_{-0.07}$ . In Figure 12, Panel a, we presented the overlaid continuum model with the spectrum. The lower sub-figure displays the residual, revealing a significant positive residual between 0.5 and 1.3 keV, with a less pronounced negative residual found between 1.4 and 2.0 keV.

Subsequently, we incorporated a CIE plasma emission model into our spectral analysis, integrating it with the continuum model, as shown in panel b of Figure 12. The best-fit temperature for the *diskbb* component was determined to be  $1.61 \pm 0.04$  keV, accompanied by a photon index for the power-law measured at  $2.80 \pm 0.07$ . The CIE component yielded a best-fit temperature of  $\log(T/\text{keV}) = 7.01 \pm 0.03$ , a best-fit column density of  $\log(N_{\text{H}}/\text{cm}^2) = 20.9 \pm 0.2$ , and a best-fit electron density of  $\log(n_e/\text{cm}^{-3}) = 13.2 \pm 0.1$ . The addition

of the CIE component notably improved the fit, although some emission residuals persisted between 0.65 and 1 keV and 1.1 and 1.2 keV (see the lower panel of 12b). Minor absorption residuals persisted within the 1.4 and 1.6 keV range. The velocity broadening was determined to be  $v_{\text{broad}} \sim 3100$  km/s. The introduction of a CIE model greatly enhanced the goodness of fit, with  $\Delta\text{C-stat} \sim 250$  compared to the continuum-only model.

Next, we integrated a PIE plasma emission/absorption model with the continuum+CIE model to fit the observed spectrum, as shown in the bottom left panel of Figure 12. The best-fit parameters for the *diskbb* temperature and power-law index were  $1.63 \pm 0.05$  keV and  $2.80^{+0.08}_{-0.09}$ , respectively. The CIE emission model parameters remained unchanged. For the PIE emission model, the best-fit parameters were  $\log \xi = 2.51 \pm 0.25$  and  $\log(N_{\text{H}}/\text{cm}^2) = 21.5 \pm 0.3$ ,  $\log(n_e/\text{cm}^{-3}) = 12.9 \pm 0.1$ , while for the PIE absorption model, the best-fit parameters were  $\log \xi = 3.50 \pm 0.25$ ,  $\log(N_{\text{H}}/\text{cm}^2) = 21.7 \pm 0.3$ , and  $\log(n_e/\text{cm}^{-3}) = 13.6 \pm 0.1$ . Absorption features were iden-

tified at energies above 1.4 keV, with a marginal blueshift of  $\sim 0.007c$  suggesting an associated wind outflow, consistent with the findings reported by Shaposhnikov et al. (2009) in their Suzaku observation of Cyg X-2. The line broadening of the emission/absorption lines was determined to be  $\sim 3400$  km/s. The addition of the PIE model further improved the fit quality with  $\Delta C\text{-stat} > 350$  compared to the continuum-only model. The fit successfully eliminated the absorption residuals, as demonstrated in the lower subfigure of Figure 12c, but slight emission residual persisted between 0.65 and 1.0 keV.

In earlier studies, reflection features were detected in Cyg X-2 within the energy range of 0.5–0.8 keV. For comprehensive modeling of the 1 keV feature in Cyg X-2, a continuum + CIE emission + PIE emission/absorption model + reflection model was utilized to fit the observed spectrum, as shown in the bottom right panel of Figure 12. The best-fit parameters for the *diskbb* and power-law index remained the same. For the CIE model, we derived the best-fit temperature to be  $\log(T/\text{keV}) = 7.11 \pm 0.03$ , best-fit column density to be  $\log(N_H/\text{cm}^2) = 20.8 \pm 0.2$ . The electron density remained unchanged. The parameters of the PIE emission/absorption model and velocity broadening values remained unchanged from the continuum + CIE + PIE emission/absorption model. For the reflection model, we assumed high electron density ( $\log(n_e/\text{cm}^{-3}) = 20$ ) and column density ( $\log(N_H/\text{cm}^2) = 23$ ) and maintained them as fixed parameters. The best-fit parameters for the reflection model were determined to be  $\log \xi = 2.1 \pm 0.1$ , an inner radius of  $\log(r_{in}/\text{cm}) = 6.50 \pm 0.18$ , and an illumination angle of  $54^\circ \pm 8^\circ$ . The fit further improved with  $\Delta C\text{-stat} > 380$  compared to the continuum-only model. The application of this combined model successfully eliminated both emission and absorption residuals, as demonstrated in the lower subfigure of Figure 12d. The contour plots displayed in Fig 1, 2, 3, 4, 5, and the linear plot displayed in Fig 6 illustrate the best-fit parameters of this final model, symbolized by red diamonds.

## 6 CONCLUSIONS

In this paper, we focused on the 1 keV feature observed in XRBs, which offers vital insights into the mechanisms governing accretion onto neutron stars or black holes, and the characteristics of super-Eddington accretion. The primary objective of our study was to present a comprehensive theoretical framework that explains the origin of the 1 keV feature along with its variability, both in terms of its centroid and intensity. We conducted a thorough analysis of emission and absorption lines under three specific conditions: photoionization equilibrium (PIE), collisional ionization equilibrium (CIE), and reflection of X-rays off the inner regions of an accretion disk. Using the spectral synthesis code *CLOUDY*, we ran grid simulations by varying the ionization parameter and column density in PIE plasmas, temperature and column density in CIE plasmas, and the ionization parameter for modeling the reflection lines. Finally, to illustrate the application of this model, we utilized it to successfully fit and explain the physics behind the 1 keV features observed in 5 XRBs, two ULXs - NGC 247 ULX-1 and NGC 1313 X-1, one X-ray pulsar - Hercules X-1, and two typical LMXBs - Cyg X-2 and Serpens X-1.

- In our *CLOUDY* simulations, we used observed SEDs from NGC 1313 X-1, NGC 247 ULX-1, Hercules X-1, Cyg X-2, and Serpens X-1, covering X-ray, optical, and UV energy ranges, as radiation sources. This study aimed to understand how variations in plasma properties influence the intensity and centroid positions of the 1 keV feature across different types of plasmas. For PIE plasma, we constructed three sets of emission line blends— $\text{Em}_{\text{blend}}$  (0.6–1.4

keV),  $\text{Em}_{\text{left}}$  (0.6–1.0 keV), and  $\text{Em}_{\text{right}}$  (1.0–1.4 keV)—and similarly, three absorption line blends— $\text{Abs}_{\text{blend}}$  (0.5–2.0 keV),  $\text{Abs}_{\text{left}}$  (0.5–1.0 keV), and  $\text{Abs}_{\text{right}}$  (1.0–2.0 keV). These were studied using logarithmic grids for  $\xi$  and  $N_H$ . For CIE plasma, we utilized identical energy ranges as the PIE emission model to construct emission line blends and analyzed them over grids for temperature and  $N_H$ . To model reflection lines, we generated three reflection line blends— $\text{Reflect}_{\text{blend}}$  (0.5–2.0 keV),  $\text{Reflect}_{\text{left}}$  (0.5–1.0 keV), and  $\text{Reflect}_{\text{right}}$  (1.0–2.0 keV). These blends were analyzed across a range of  $\xi$  values, with a particularly high column density ( $N_H = 10^{23} \text{ cm}^{-2}$ ) assigned to simulate conditions typical of dense astrophysical environments.

- We effectively describe the origin and variation of the 1 keV feature across a diverse range of X-ray binaries using *XMM-Newton*/RGS and *NICER* observations. The 1 keV feature in NGC 1313 X-1 was best modeled by a combination of a two-blackbody continuum and a PIE emission/absorption model, which yielded the most precise fit to the spectra. NGC 247 ULX-1 necessitated a two-blackbody continuum + PIE emission/absorption + CIE emission model for effectively modeling the 1 keV feature. In the case of NGC 247 ULX-1, we found that an effective model for accurately representing the 1 keV feature required incorporating a combination of a two-blackbody continuum, PIE emission/absorption, and CIE emission. Similarly, in Hercules X-1, the integration of a blackbody+powerlaw continuum, CIE emission, and PIE emission/absorption models effectively eliminated the residuals at 1 keV. For Cyg X-2, achieving a thorough modeling of the 1 keV feature required integrating reflection lines from the inner accretion disk, PIE emission/absorption, and CIE emission components, in addition to the disk blackbody component and a power-law component utilized for modeling the continuum. For Serpens X-1, effectively eliminating the 1 keV residual required a combination of blackbody and disk blackbody continuum components, along with PIE emission and reflection lines.

- A complete list of all the lines within the 1 keV emission, absorption, and reflection feature across the entire parameter space explored in this paper, both bright and faint, has been listed in Table 2. The instruction to generate PIE emission/absorption, CIE emission and reflection line blends have been discussed in the appendix.

- This paper revisits systems previously analyzed, with the current study focused on understanding the physical processes responsible for the origin and variability of the 1 keV feature, a novel aspect of this work. Unlike prior studies that detailed the properties and geometries of these systems, our research is specifically aimed at investigating the atomic origin of the 1 keV feature. All our fittings were conducted using *CLOUDY*, and we observed that our results were largely consistent with those of previous studies, which used codes such as *SPEX* (Kaastra et al. 1996) and *RELXILL* (García et al. 2014), although there were some minor discrepancies. Pinto et al. (2020) modeled the intermediate-bright state of NGC 1313 X-1 using a PIE emission/absorption model implemented through *SPEX*. Similarly, our analysis of the same observation using the *CLOUDY* model, which also required a PIE emission/absorption approach, yielded ionization parameters and column densities that closely align with those reported in the prior study. The data for NGC 247 ULX-1, previously fitted with separate CIE and PIE models by Pinto et al. (2021), highlighted the need for more complex models to interpret the 1 keV features. Our results indicate that a combined CIE and PIE model approach fits the residuals more effectively, though this difference may be attributed to our deliberate omission of a CIE absorption model, as the absorption is predominantly linked to photoionized winds in XRBs (Higginbottom & Proga 2015). In their

study of Her X-1, [Kosec et al. \(2022\)](#) modeled the 1 keV spectral feature using a Gaussian profile with a width between 0.35 and 0.4 keV. They emphasized the necessity of applying physical modeling to fully comprehend the nature of this feature. In this work, we utilize a combination of CIE emission and PIE emission/absorption models to adequately fit this spectral feature. In modeling the Fe L complex reflection feature near 1 keV for Ser X-1, [Ludlam et al. \(2018\)](#) used the RELXILLNS reflection model but noted persistent residuals between 0.5-0.9 keV. We addressed the residuals around 1 keV using a combination of reflection emission lines and a PIE emission model, finding our parameters for ionization, illumination angle, and inner disk radius consistent with those reported by [Ludlam et al. \(2018\)](#) for the reflection feature. For Cyg X-1, [Ludlam et al. \(2022\)](#) applied RELXILLNS and the CIE emission model MEKAL ([Liedahl et al. 1995](#)) to model the 1 keV feature, but slight absorption residuals remained. We incorporated a PIE model to address the absorption, complementing it with CIE and reflection models to achieve a spectrum fit with minimal residuals. The temperature of our CIE model was in agreement with that of the MEKAL model, and the parameters for ionization, illumination angle, and inner disk radius were in agreement with the findings reported by [Ludlam et al. \(2022\)](#) for the reflection model.

## APPENDIX

Here, we describe the CLOUDY commands used in our study of the 1 keV feature. The SED for each source was determined using the command:

```
Table sed "input.txt"
```

with the input SEDs corresponding to the observed SEDs discussed in Section 3. We used the blend command, described in [Ferland et al. \(2017\)](#) in Section 2.3.2, to define line blends of the lines listed in Table 2. We created two line blends blend 11 for lines with energies > 1 keV, and blend 13 for lines with energies < 1 keV listed in table 2. For creating line blends the command we used in CLOUDY was:

```
set blend 11
Mg12 6.58008
Al12 6.63476
Si13 6.64803
Si13 6.68827
Si13 6.74039
Mg11 7.03734
Mg12 7.10615
Al13 7.17271
Mg11 7.31028
Mg11 7.47313
Al12 7.75730
Mg11 7.85052
Fe20 7.86906
Fe20 8.20998
Fe20 8.27000
Fe20 8.31000
Mg12 8.42100
Fe20 8.44003
Fe20 8.46002
Fe19 8.49473
Fe20 8.50000
Fe20 8.69996
Fe22 8.71500
Fe22 8.72200
```

```
Fe20 8.74004
Fe20 8.77001
Fe19 8.81003
Fe21 8.84000
Fe21 8.85500
Fe21 8.89800
Fe20 8.89996
Fe19 8.91997
Fe19 8.91997
Fe20 8.93001
Fe19 8.93001
Fe19 8.96001
Fe22 8.97700
Fe19 9.03000
Fe20 9.06500
Fe20 9.06900
Fe20 9.06900
Fe19 9.06997
Fe19 9.06997
Fe19 9.06997
Fe22 9.07300
Fe20 9.11000
Fe20 9.11000
Fe22 9.12200
Fe21 9.14000
Fe22 9.14800
Fe20 9.16300
Mg11 9.16875
Fe20 9.18400
Fe19 9.18999
Fe19 9.19997
Fe19 9.19997
Fe20 9.21600
Fe20 9.21600
Fe19 9.21999
Fe20 9.22000
Fe20 9.22000
Fe19 9.23003
Fe19 9.23003
Mg11 9.23121
Fe20 9.25800
Fe20 9.28100
Mg11 9.31434
Fe19 9.32001
Fe19 9.32001
Fe20 9.32500
Ni25 9.33000
Fe19 9.33001
Ne10 9.36162
Ni20 9.37700
Ni20 9.38500
Fe19 9.45001
Ni20 9.45500
Fe21 9.47500
Ne10 9.48075
Fe21 9.48200
Fe21 9.54200
Fe21 9.54800
Ni20 9.55800
Ni20 9.55900
Fe21 9.58200
Fe21 9.58700
```

Fe19 9.63900	Fe18 11.42000
Fe21 9.69000	Fe22 11.44200
Fe19 9.69100	Fe22 11.45900
Fe19 9.69100	Ni21 11.46800
Fe21 9.70000	Fe23 11.48500
Fe21 9.70500	Fe22 11.51000
Ne10 9.70818	Ni21 11.51600
Fe19 9.72600	Ni21 11.51700
Fe21 9.82100	Fe18 11.52500
Fe19 9.84800	Fe18 11.52500
Fe19 9.85200	Ni21 11.53900
Fe19 9.88800	Ni19 11.53900
Na11 10.02500	Ne 9 11.54660
Fe18 10.08000	Mn23 11.57660
Ni19 10.11000	Ni21 11.59700
Ne10 10.23890	Fe22 11.59900
Fe18 10.41000	Fe22 11.66900
Fe18 10.41000	Fe23 11.71800
Fe23 10.50600	Fe23 11.73700
Fe18 10.52600	Fe20 11.73900
Fe24 10.61900	Fe22 11.76800
Fe19 10.63200	Ni20 11.78700
Fe19 10.63200	Ni20 11.83200
Fe19 10.63300	Ni20 11.84100
Fe19 10.65500	Fe23 11.84600
Fe19 10.65700	Ni20 11.86500
Fe24 10.66300	Ni20 11.87400
Fe19 10.68400	Fe22 11.92100
Fe19 10.70200	Fe20 11.93300
Cr20 10.71200	Fe22 11.93400
Fe19 10.74400	Fe21 11.93800
Fe19 10.75800	Ni20 11.96100
Fe19 10.76000	Mn22 11.97000
Fe19 10.76000	Fe21 11.97500
Ni20 10.77200	Ni20 11.97800
Fe19 10.80500	Fe20 11.98700
Fe19 10.80500	Ca18 11.98900
Fe19 10.81600	Ni20 11.99100
Fe19 10.82700	Ni20 11.99100
Fe19 10.82700	Mn22 11.99800
Fe19 10.88000	Ni20 12.00600
Fe19 10.91600	Ti19 12.01000
Fe19 10.93300	Fe23 12.02700
Fe19 10.93300	Fe21 12.04400
Fe23 10.98000	Ni20 12.04700
Na10 11.00260	Ni20 12.08100
Fe23 11.01800	Fe21 12.08200
Ni20 11.13800	Fe21 12.10700
Ni20 11.13800	Ni20 12.11200
Ni20 11.15800	Ni20 12.13000
Ni20 11.22600	Ne10 12.13390
Ni20 11.22600	end of blend 11
Ni21 11.22700	
Ni21 11.24100	
Ni21 11.24200	
Ni21 11.27200	set blend 13
Ni20 11.28200	Fe21 12.14600
Ni21 11.30200	Ni20 12.15700
Ni21 11.31900	Fe23 12.16100
Fe18 11.32600	Ni21 12.16500
Fe18 11.32600	Fe22 12.19300
Ni21 11.38000	Ni21 12.20900



Fe21	12.26100	Fe20	12.96600
Ni21	12.27600	Fe20	12.98200
Fe21	12.28200	Fe20	12.99100
Fe21	12.29700	Fe19	13.01800
Fe21	12.32700	Ni20	13.03200
Fe21	12.32700	Fe19	13.03900
Fe23	12.35100	Fe20	13.04400
Fe21	12.39500	Fe20	13.04600
Fe21	12.42200	Fe19	13.05100
Fe20	12.42600	Fe20	13.05200
Fe20	12.42600	Fe21	13.05200
Ni19	12.43500	Fe20	13.05900
Fe23	12.44400	Fe19	13.07500
Ni21	12.44600	Fe19	13.07500
Fe21	12.46200	Ni20	13.07500
Ni21	12.47200	Fe20	13.07800
Fe21	12.49000	Fe20	13.09100
Fe21	12.49200	Fe19	13.09100
Fe23	12.49300	Fe20	13.09100
Fe21	12.49900	Fe19	13.09100
Fe21	12.50000	Fe20	13.11400
Fe21	12.52300	Fe20	13.11400
Fe21	12.52300	Fe20	13.12300
Fe21	12.53300	Cr21	13.12300
Ni21	12.53300	Fe20	13.14000
Fe20	12.56600	Fe20	13.14300
Fe21	12.56800	Fe21	13.17900
Fe20	12.58100	Fe20	13.18800
Fe20	12.58100	Fe20	13.20300
Ni21	12.59100	Fe20	13.20600
Cr22	12.61300	Fe19	13.21200
Fe21	12.62300	Fe19	13.21200
Ca18	12.63600	Fe19	13.21200
Ca18	12.63600	Fe20	13.25300
Ni21	12.64800	Fe20	13.25400
Fe23	12.65300	Fe19	13.25400
Cr22	12.65500	Fe21	13.25500
Ni19	12.65600	Ni20	13.25600
Fe21	12.66300	Fe20	13.26700
Fe21	12.69100	Fe20	13.26700
Fe21	12.70100	Fe20	13.26900
Fe23	12.70300	Fe20	13.27000
Fe22	12.74300	Ni20	13.28200
Fe20	12.75300	Fe20	13.29200
Fe21	12.77200	Fe20	13.30100
Fe20	12.80400	Fe19	13.31100
Fe20	12.80400	Fe18	13.31900
Fe20	12.81200	Fe18	13.31900
Fe18	12.81800	Fe19	13.32700
Fe21	12.82200	Fe20	13.33300
Fe20	12.82400	Fe19	13.33600
Fe20	12.82700	Fe18	13.35500
Fe20	12.84500	Fe20	13.35900
Fe21	12.87000	Fe22	13.36100
Fe20	12.90500	Fe20	13.36600
Fe19	12.92400	Fe18	13.37400
Fe19	12.92400	Fe20	13.37900
Fe19	12.92400	Fe20	13.38200
Ni20	12.92700	Fe18	13.39700
Fe22	12.93600	Fe20	13.40200
Fe20	12.95100	Fe20	13.40500
Fe20	12.96600	Fe20	13.41900

Fe18	13.42400	Fe18	13.96200
Fe19	13.43000	Fe19	13.96400
Ne 9	13.44710	Fe19	13.97000
Fe19	13.45600	Fe20	13.97200
Ca17	13.46000	Fe21	14.00800
Fe19	13.46200	Fe19	14.01700
Fe18	13.46400	Ni19	14.04000
Fe20	13.46700	Ca18	14.04900
Fe19	13.47100	Ca18	14.05900
Fe21	13.48200	Fe19	14.07100
Fe19	13.50600	Fe19	14.08600
Fe19	13.50700	Fe19	14.08600
Fe20	13.51700	Fe19	14.11400
Fe19	13.52500	Fe19	14.11400
Fe20	13.53300	Fe20	14.11500
Fe20	13.55300	Fe20	14.12300
Fe19	13.55400	Fe18	14.12400
Fe19	13.55500	Fe19	14.12700
Fe19	13.55700	Fe19	14.12800
Fe21	13.57400	Fe18	14.13600
Fe22	13.61700	Fe18	14.14400
Fe19	13.62000	Fe19	14.17500
Fe19	13.62100	Fe20	14.19000
Fe19	13.63400	Fe18	14.20400
Fe19	13.63600	Fe18	14.20900
Fe19	13.64300	Cr21	14.24500
Fe19	13.64600	Fe20	14.24800
Fe19	13.64800	Fe19	14.25200
Fe20	13.67000	Fe18	14.25800
Fe19	13.67200	Fe18	14.25800
Fe19	13.67200	Fe18	14.34400
Fe19	13.67300	Fe18	14.35200
Fe22	13.67400	V 20	14.35960
Fe19	13.69100	Fe18	14.37300
Fe19	13.69400	Fe18	14.41900
Fe21	13.71700	Fe18	14.41900
Fe19	13.72000	Fe18	14.45300
Fe19	13.72100	Fe18	14.47000
Fe19	13.72100	Fe18	14.48700
Fe19	13.74100	Fe20	14.49300
Fe19	13.75400	Fe20	14.50000
Fe19	13.76200	Fe18	14.53700
Fe19	13.76900	Fe18	14.55100
Fe22	13.77100	Fe19	14.57000
Ni19	13.77800	Fe18	14.58000
Fe20	13.78100	Fe18	14.61000
Fe19	13.79200	O 8	14.63430
Fe19	13.79900	Fe19	14.66400
Fe19	13.82200	Fe19	14.66900
Fe19	13.82200	Fe18	14.67100
Fe19	13.84100	Fe19	14.69400
Fe19	13.84300	Fe19	14.73800
Fe19	13.84400	Fe19	14.74100
Fe20	13.84400	Fe20	14.76400
Fe19	13.87100	Fe18	14.77100
Fe19	13.87200	O 8	14.82060
Fe19	13.93600	Fe19	14.86800
Fe19	13.93800	Fe20	14.91300
Fe19	13.93800	Fe21	14.91600
Fe19	13.93800	Fe19	14.93200
Fe19	13.94200	Fe20	14.93200
Fe19	13.95700	Fe19	14.93500

Ca17 14.94000  
 Fe19 14.99200  
 Fe19 14.99200  
 Fe17 15.01300  
 Fe19 15.04200  
 Fe20 15.06000  
 Fe20 15.06300  
 Fe19 15.08100  
 Fe19 15.11400  
 Fe19 15.16300  
 O 8 15.17620  
 Ar16 15.19000  
 Fe19 15.19600  
 Fe19 15.20800  
 Ti20 15.21100  
 Ti20 15.25300  
 Fe17 15.26200  
 Fe19 15.33000  
 Fe19 15.35200  
 Fe20 15.51500  
 Fe18 15.62200  
 Fe18 15.76600  
 Fe18 15.82800  
 Ti19 15.86500  
 Ar16 15.93300  
 Fe18 16.00500  
 O 8 16.00590  
 Fe18 16.02600  
 Fe18 16.07200  
 Fe19 16.11000  
 Fe19 16.27200  
 Fe19 16.34000  
 Ti18 17.31760  
 Ar16 17.73700  
 Ar16 17.74700  
 Ca18 18.69100  
 S 14 18.72000  
 Ca18 18.73200  
 O 8 18.96890  
 Ca17 19.55800  
 S 14 19.69000  
 N 7 19.82580  
 Ca17 20.4340  
 Ca16 20.8590  
 K 17 20.8990  
 N 7 20.9098  
 K 17 20.9310  
 Ca16 20.9510  
 Ca16 21.0200  
 Ca16 21.1130  
 Ca16 21.4500  
 O 7 21.6020  
 Ca16 21.6100  
 Ca16 21.6190  
 K 16 21.9110  
 Ca15 22.7300  
 Ca15 22.7300  
 Ca15 22.7590  
 Ca15 22.7770  
 Ca15 22.8210  
 S 14 23.0050  
 S 14 23.0150

Ca17 23.1750

Ca17 23.1750

Ar16 23.5060

Ar16 23.5460

Ne10 24.2678

S 13 24.5900

Ar15 24.7370

N 7 24.7810

end of blend 13

The blend appears as a new emission lines with the label blnd and wavelengths of 11Å and 13Å. We chose the blends' wavelengths of 11Å and 13Å rather than the energy 1 keV to make it easier to identify in the emission-line output.

In previous versions of CLOUDY (up to C23 or earlier), we only used experimental energy values sourced from the Chianti database due to their superior accuracy (Lykins et al. 2013). In the upcoming release, C24, there will be an option to incorporate theoretical energy values for instances where experimental data are absent. The CLOUDY command to use such a 'mixed' case is:

Database Chianti mixed

Nevertheless, for the 1 keV feature, the impact of this change appears to be minimal, as the newly introduced lines in the 1 keV range are faint, making little difference in their overall intensities.

The emitted line blends were saved with the command:

save emitted continuum

The reflected line blends were saved with the command:

save reflected continuum

The inner accretion disk radius can be specified using the following command (for example):

radius 6.5 # log of inner radius in cm

The illumination angle can be specified using the following command (for example):

illumination angle 45 deg

## ACKNOWLEDGEMENTS

GJF acknowledges support by JWST through AR6428, AR6419 GO5354, and GO5018.

## DATA AVAILABILITY

The data underlying this article will be shared on reasonable request to the corresponding author.

## REFERENCES

- Arnaud K. A., 1996, in Jacoby G. H., Barnes J., eds, *Astronomical Society of the Pacific Conference Series Vol. 101, Astronomical Data Analysis Software and Systems V*. p. 17  
 Asai K., Dotani T., Nagase F., Mitsuda K., 2000, *ApJS*, **131**, 571  
 Bhattacharyya S., Strohmayer T. E., 2007, *ApJ*, **664**, L103  
 Bowyer S., Byram E. T., Chubb T. A., Friedman H., 1965, *Science*, **147**, 394  
 Cackett E. M., Miller J. M., Raymond J., Homan J., van der Klis M., Méndez M., Steeghs D., Wijnands R., 2008, *ApJ*, **677**, 1233  
 Cackett E. M., et al., 2010, *ApJ*, **720**, 205  
 Cash W., 1979, *ApJ*, **228**, 939  
 Cowley A. P., Crampton D., Hutchings J. B., 1979, *ApJ*, **231**, 539  
 Di Salvo T., et al., 2002, *A&A*, **386**, 535  
 Fabrika S. N., Atapin K. E., Vinokurov A. S., Sholukhova O. N., 2021, *Astrophysical Bulletin*, **76**, 6  
 Feigelson E. D., 1975, *Nature*, **253**, 250

- Feng H., Tao L., Kaaret P., Grisé F., 2016, [ApJ](#), **831**, 117
- Ferland G. J., et al., 2017, [Rev. Mex. Astron. Astrofis.](#), **53**, 385
- García J., et al., 2014, [ApJ](#), **782**, 76
- HI4PI Collaboration et al., 2016, [A&A](#), **594**, A116
- Higginbottom N., Proga D., 2015, [ApJ](#), **807**, 107
- Iaria R., et al., 2016, [A&A](#), **596**, A21
- Jiang J., et al., 2019, [MNRAS](#), **489**, 3436
- Jin J., Feng H., Kaaret P., Zhang S.-N., 2011, [ApJ](#), **737**, 87
- Kaastra J. S., Mewe R., Nieuwenhuijzen H., 1996, in *UV and X-ray Spectroscopy of Astrophysical and Laboratory Plasmas*. pp 411–414
- Koljonen K. I. I., Tomsick J. A., 2020, [A&A](#), **639**, A13
- Kosec P., et al., 2021, [MNRAS](#), **508**, 3569
- Kosec P., et al., 2022, [ApJ](#), **936**, 185
- Liedahl D. A., Osterheld A. L., Goldstein W. H., 1995, [ApJ](#), **438**, L115
- Ludlam R. M., et al., 2018, [ApJ](#), **858**, L5
- Ludlam R. M., et al., 2022, [ApJ](#), **927**, 112
- Lykins M. L., Ferland G. J., Porter R. L., van Hoof P. A. M., Williams R. J. R., Gnat O., 2013, [MNRAS](#), **429**, 3133
- Malacaria C., et al., 2023, [A&A](#), **669**, A38
- Middleton M. J., Walton D. J., Roberts T. P., Heil L., 2014, [MNRAS](#), **438**, L51
- Middleton M. J., Walton D. J., Fabian A., Roberts T. P., Heil L., Pinto C., Anderson G., Sutton A., 2015, [MNRAS](#), **454**, 3134
- Miller J. M., Fabbiano G., Miller M. C., Fabian A. C., 2003, [ApJ](#), **585**, L37
- Miller J. M., et al., 2013, [ApJ](#), **779**, L2
- Mondal A. S., Dewangan G. C., Raychaudhuri B., 2020, [MNRAS](#), **494**, 3177
- Oegelman H., Kahabka P., Pietsch W., Truemper J., Voges W., 1985, [Space Sci. Rev.](#), **40**, 347
- Oosterbroek T., Parmar A. N., Martin D. D. E., Lammers U., 1997, [A&A](#), **327**, 215
- Oosterbroek T., Parmar A. N., Orlandini M., Segreto A., Santangelo A., Del Sordo S., 2001, [A&A](#), **375**, 922
- Paul B., Nagase F., Endo T., Dotani T., Yokogawa J., Nishiuchi M., 2002, [ApJ](#), **579**, 411
- Pinto C., Middleton M. J., Fabian A. C., 2016, [Nature](#), **533**, 64
- Pinto C., Fabian A., Middleton M., Walton D., 2017, [Astronomische Nachrichten](#), **338**, 234
- Pinto C., et al., 2020, [MNRAS](#), **492**, 4646
- Pinto C., et al., 2021, [MNRAS](#), **505**, 5058
- Remillard R. A., et al., 2022, [AJ](#), **163**, 130
- Roberts T. P., Kilgard R. E., Warwick R. S., Goad M. R., Ward M. J., 2006, [MNRAS](#), **371**, 1877
- Schwöpe A., Marsh T. R., Standke A., Pelisoli I., Potter S., Buckley D., Munday J., Dhillon V., 2023, [A&A](#), **674**, L9
- Shaposhnikov N., Titarchuk L., Laurent P., 2009, [ApJ](#), **699**, 1223
- Smale A. P., 1998, [ApJ](#), **498**, L141
- Stobart A. M., Roberts T. P., Wilms J., 2006, [MNRAS](#), **368**, 397
- Swank J. H., Becker R. H., Pravdo S. H., Saba J. R., Serlemitsos P. J., 1976, [IAU Circ.](#), **3000**, 5
- Tananbaum H., Gursky H., Kellogg E. M., Levinson R., Schreier E., Giacconi R., 1972, [ApJ](#), **174**, L143
- Turner M. J. L., et al., 2001, [A&A](#), **365**, L27
- Vinokurov A., Fabrika S., Atapin K., 2013, [Astrophysical Bulletin](#), **68**, 139
- Vrtilek S. D., Kahn S. M., Grindlay J. E., Helfand D. J., Seward F. D., 1986, [ApJ](#), **307**, 698
- Walton D. J., et al., 2020, [MNRAS](#), **494**, 6012
- Wang C., Soria R., Wang J., 2019, [ApJ](#), **883**, 44
- Winter L. M., Mushotzky R. F., Reynolds C. S., 2006, [ApJ](#), **649**, 730
- den Herder J. W., et al., 2001, [A&A](#), **365**, L7

This paper has been typeset from a  $\text{\LaTeX}$  file prepared by the author.